J. Fluid Mech. (1979), *vol.* 95, *part* 2, *pp.* 279–304
Printed in Great Britain

An experimental study of liquefaction shock waves

By GEORG DETTLEFF, PHILIP A. THOMPSON,†
GERD E. A. MEIER AND HANS-DIETER SPECKMANN

Max-Planck-Institut für Strömungsforschung, D 3400 Göttingen

(Received 12 September 1978 and in revised form 19 December 1978)

The existence of a liquefaction shock wave, a compression shock which converts vapour into liquid, has recently been predicted on physical grounds. The liquefaction shock was experimentally produced as the reflected shock at the closed end of a shock tube. Measurements of pressure, temperature, index of refraction and shock velocity confirm the existence of the shock and its general conformity to classical Rankine–Hugoniot conditions, with a discrepancy $\sim 10\,^{\circ}\mathrm{C}$ between measured and predicted liquid temperatures. Photographic observations confirmed the existence of a clear liquid phase and revealed the (unanticipated) presence of small two-phase torus-form rings. These rings are interpreted as vortices and are formed in or near the shockfront (~ 50 rings/mm^2 are visible near the shockfront at any given time). Separate experiments with the incident shock under conditions of *partial* liquefaction produced a fog behind the shock: measurements of laser-beam attenuation yielded the thickness of the condensation zone and estimates of the droplet size ($\sim 10^{-7}$ m).

1. Introduction

A liquefaction shock wave is a compression discontinuity for which the upstream state is vapour and the downstream state is liquid. Viewed macroscopically, the shockfront is also a surface of phase discontinuity.

The liquefaction shock is thus a new phenomenon, quite distinct from the well-known condensation of vapour in an expanding flow, for example in a supersonic nozzle (Wegener & Wu 1976; Blythe & Shih 1976, among many others): this form of rapid condensation is invariably associated with a supersaturated state achieved by adiabatic expansion. Under certain conditions it leads to development of a recompression shock wave sometimes called a 'condensation shock'. In order to distinguish clearly the subject of this paper from such shock waves, we have chosen the distinct name 'liquefaction shock'. Unfortunately, the name 'complete condensation shock' was used in the title of the work of Thompson & Sullivan (1975), which describes the elementary theory for the liquefaction shock.

The definition for a liquefaction shock given above implies the complete liquefaction of a superheated vapour, i.e. a complete transition from gas to liquid across the shock. Depending on experimental conditions, it is of course possible that either the upstream state or the downstream state, or both, consist of a mixture of both phases. In the experiments reported here, all combinations of state have been found: the emphasis is, however, on the complete liquefaction shock, and to a lesser extent on the partial

† Present address: Department of Mechanical Engineering, Rensselaer Polytechnic Institute, Troy, N.Y. 12181.

0022-1120/79/4272-7280 $02.00

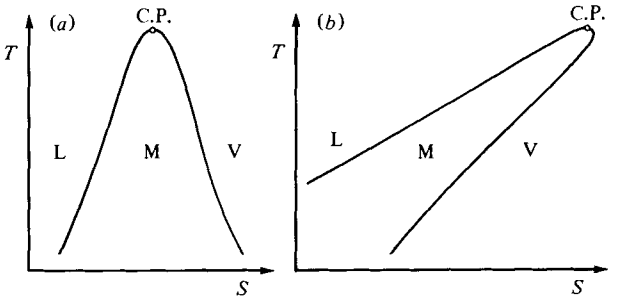

FIGURE 1. Temperature–entropy diagrams for regular and retrograde substances. (*a*) Regular substance (water); (*b*) retrograde substance (normal octane). An isentropic compression corresponds to a vertical path with increasing temperature; an isentropic expansion corresponds to a vertical path with decreasing temperature. The liquid, mixture and vapour regions are designated by L, M and V respectively. C.P. designates the critical point. (Redrawn from Thompson & Sullivan 1975.)

liquefaction shock for which the downstream fluid is a mixture of liquid droplets and gas, i.e. a fog. In the majority of the experiments, the upstream fluid was a dry vapour.

The physical basis for the liquefaction shock. This can be easily understood, thinking of the shock process as a roughly adiabatic compression. Such a compression will, if carried far enough, inevitably lead to liquefaction of the gas, provided that the gas temperature shows only a modest increase. This will indeed be the case if the gas molecules have a large number of vibrational degrees of freedom (i.e. the gas has a large molar heat capacity) so that the work of compression can be stored as internal energy in the gas with only a correspondingly small temperature rise. It is instructive in this connexion to think of an isentropic compression in a perfect gas for which $T \sim P^{(\gamma-1)/\gamma}$: as $\gamma \to 1$, $T \to$ constant. After the onset of liquefaction, similar arguments apply to the storage of the latent heat released by condensation, i.e. the temperature rise will again be small if the molar heat capacity is large.

The detailed calculations of Thompson & Sullivan (1975) yield minimum values for the heat capacity which allow liquefaction. These are conveniently expressed in terms of a standard heat capacity $\tilde{c}_v \equiv c_v^0(T_c)/R$, the normalized ideal-gas heat capacity evaluated at the critical temperature for the substance of interest. Partial shock liquefaction is possible for $\tilde{c}_v > 11{\cdot}2$ and complete shock liquefaction is possible for $\tilde{c}_v > 24{\cdot}1$: the former value happens to correspond to sulphur hexafluoride SF_6 and the latter value corresponds roughly to hexane C_6H_{14}.

Substances with $\tilde{c}_v < 11{\cdot}2$, for which isentropic condensation of the vapour is only possible in an expansion process, are referred to as *regular*: an example is water H_2O ($\tilde{c}_v = 3{\cdot}5$). Substances with $\tilde{c}_v > 11{\cdot}2$, for which isentropic condensation of the vapour is possible in a compression process, are referred to as *retrograde*: an example is normal octane C_8H_{18} ($\tilde{c}_v = 36{\cdot}8$). Regular and retrograde behaviour are illustrated in figure 1. It should be remarked that the establishment of a limiting value $\tilde{c}_v = 11{\cdot}2$ for retrograde behaviour, and of similar limits, is based on the assumption of a particular kind of corresponding-states thermodynamic behaviour, and therefore represents an approximation. The corresponding-states model used is explicitly described by Thompson & Becker (1979).

Virtually all previous spontaneous condensation experiments of which we are aware

have involved states of supersaturation reached in an expansion process, using regular fluids (mainly water) or, occasionally, slightly retrograde fluids (such as benzene), but in such a way that the retrograde property was not relevant. These experiments extend back at least to the time of Wilson (1897*a*, *b*): a useful summary for water is given by Wegener (1969).

In view of this extensive experience, devoted exclusively to expansion condensation, it is perhaps not surprising that the intuitively plausible possibility of compression condensation is dismissed outright or regarded with scepticism. Landau & Lifshitz (1959) make the following comment about the possibility of a liquefaction shock wave:

> It should be emphasized that condensation discontinuities are a distinct physical phenomenon, and do not result from the compression of gas in an ordinary shock wave; the latter effect cannot lead to condensation, since the increase of pressure in the shock wave has less effect on the degree of supersaturation than the increase of temperature...

This argument corresponds to the physical basis discussed in the preceding, but is incomplete, leading to an incorrect conclusion.

Previous investigations. Saltanov, Tsiklauri & Shanin (1970) reported experimental results on the shock compression of a very wet liquid–vapour mixture (water), with condensation of the vapour fraction ($\sim 10\,\%$). In an experiment carried out at the California Institute of Technology, Sturtevant (1970) found scattering of laser light on the downstream side of a shock in Freon 113 ($\tilde{c}_v = 17{\cdot}4$), indicating the presence of condensate droplets. Dettleff, Thompson & Meier (1976) gave an account of preliminary experiments indicating the existence of liquefaction shock waves.

Among the several studies of particulate condensation in supersaturated metal vapours, that of Homer (1971) is remarkable in that he apparently found condensation of lead immediately behind a shock wave. The lead vapour was produced by pyrolysis of tetramethyl-lead highly diluted in argon.

Aim of the experimental study. The experiments reported here had three main objectives: first, the establishment of the existence of the liquefaction shock; second, the determination of the extent to which the shock transition agrees with the predictions of classical shock-discontinuity theory (i.e. the Rankine–Hugoniot equations) as described by Thompson & Sullivan (1975), third, to observe whatever phenomena might arise in the shock process.

To a considerable extent these objectives may be regarded as having been met, the first one in particular. It will be seen, however, that questions of interest remain.

2. Experimental arrangement

The experiments were carried out in a cylindrical shock tube. Following the suggestion of Thompson & Sullivan (1975) the experiment was arranged to produce the liquefaction shock as the reflected shock from the closed end of the shock tube test section, as shown in the hypothetical x, t wave diagram in figure 2. Because the density in the liquid state (2) is large, the reflected liquefaction shock travels slowly away from the end wall, reaching a maximum distance ~ 2 cm from the end wall. Under these conditions, experimental observation of the shock is convenient.

Many experimental details not given here can be found in the work of Dettleff (1978) and of Speckmann (1978).

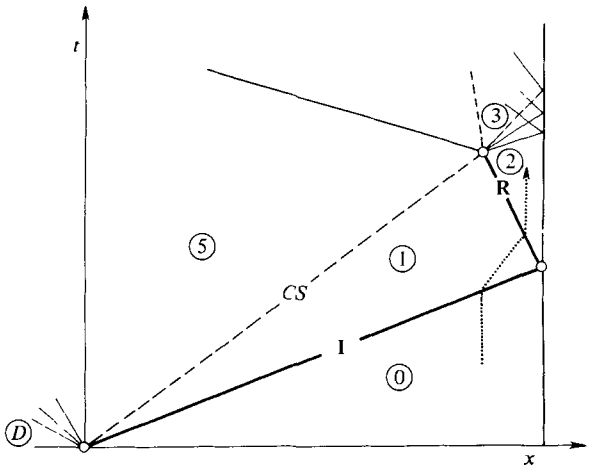

FIGURE 2. Hypothetical x, t wave diagram for the shock-tube flow. The closed end of the test section is at the right. Arabic numerals designate fluid states. Other designations: **I**, incident shock; **R**, reflected (liquefaction) shock; *CS*, contact surface; *D*, driver gas initial state. Not to scale.

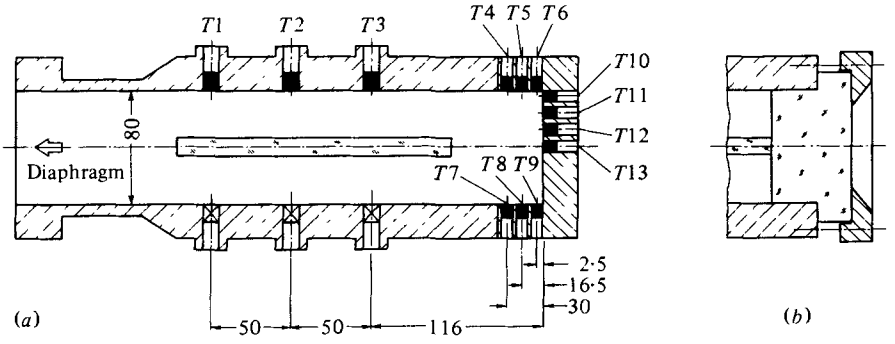

FIGURE 3. Observation section of the shock tube. The designations $T1$ to $T13$ refer to the transducer locations. Dimensions in mm.

Shock tube. The driver section is 2·50 m long, the test section 2·426 m long. The shock tube is made of brass, with a wall thickness of 5 mm and internal diameter of 80 mm. In order to allow stable initial temperatures up to $T_0 = 160\,^{\circ}\mathrm{C}$, the shock tube was surrounded with electrical resistance heating wire and covered with flexible asbestos foam insulation with a total thickness $\sim$ 60 mm.

The diaphragm material was Dupont 'Capton' polyamide, in various thicknesses and combinations in the range 25–300 μm. Diaphragm burst could be initiated by an arrowhead plunger mounted on the driver-section side of the diaphragm; this plunger was released by an electrical signal.

Most of the measuring sensors are mounted in the *observation section*, which forms the final 300 mm length of the shock tube, as shown in figure 3. Almost all of the shock measurements, on both partial and complete liquefaction shocks, were carried out here. Two distinct window arrangements are available for optical measurements and photography: narrow side windows 12 × 180 mm permit a transverse view through the observation section, and a large circular end window, with inner frame diameter 70

Formula	Name	$\tilde{M}$	T_b (°C)	T_c (°C)	P_c (bar)	$\tilde{c}_v$	ρ_l (g/cm^3)†
C_8F_{16}	PP3	400	102	241·5	19·2	53·9	1·84
$C_{11}F_{20}$	PP9	512	160	313·4	16·9	73·4	1·98
—	FC40	650	150	277·0	14·8	90·0	1·87

† ρ_l is the saturated-liquid density at 20 °C.

TABLE 1. Test fluids.

mm (in a few experiments, 50 mm) can be mounted as shown in figure 3(*b*) to replace the metal end plate (with this window in place, the test section length is reduced to 2·360 m). The transducer mounting locations $T1$ to $T13$ can be used for pressure transducers, temperature probes, or other devices.

Test fluids. Three different retrograde substances, all fluorocarbons, were used in the experiments: C_8F_{16} (ISC Ltd designation PP3), $C_{11}F_{20}$ (ISC Ltd designation PP9) and a substance of unknown chemical composition, but described by the manufacturer as similar to $(C_4F_9)_3N$ (MMM Co. designation FC40). The two ISC substances PP3 and PP9 are cyclic compounds, perfluoro-dimethylcyclohexane and perfluoro-methyl-decalin, respectively. Properties as given by the manufacturers are summarized in table 1.

The advantage of using fluorinated substances is that they do not present any health hazards and are not flammable; the disadvantage is their relatively high cost. With reasonable precautions, there would be no difficulty in using hydrocarbons such as, say, normal decane $C_{10}H_{22}$, nor is there any reason to expect that the experimental results would be significantly different.

The majority of the experiments reported here were performed with PP3. None of the test substances was of high purity. PP3 and PP9 consisted of $\sim$ 90 % of the nominal compounds, the remainder being mainly related compounds with one carbon atom more or less; virtually no hydrocarbons were present. No information was available on the purity of FC40; there are indications (e.g. the vapour pressure) that it was low. No attempt was made to improve the purity, by freezing or otherwise. Each sample was degassed before use, by heating under intermittent exposure to vacuum.

Experimental procedure. The shock tube was kept continuously heated in order to hold the steady initial temperature T_0. After mounting the diaphragm, the test section was evacuated to a pressure less than 10^{-2} torr. The desired quantity of degassed test fluid was drawn into an evacuated sample bottle and weighed on a balance: the test fluid was then drawn into the evacuated test section. Because the last portion of liquid drawn into the test section could not be visually observed, it was not certain that all of the measured mass m_0 went into the tube. The initial state (0) was therefore based on the pressure P_0, measured with a Kistler 7261 quartz piezoelectric transducer (decay time $\sim$ 30 min), and on the temperature T_0, measured with the temperature-control thermocouples in the tube wall and with an independent miniature thermocouple inside the tube; the measured pressure P_0 was found in every case to be consistent with that calculated from the equation of state for $P_0 = P_0(T_0, m_0/V)$, where V is the volume of the test section.

After the filling was complete and the triggering, measuring and recording devices had been prepared, the driver section was pressurized with nitrogen driver gas from a

m_0, P_0, T_0	initial-state properties
$P(t)$, $T(t)$	static pressure and temperature
$I(t)$	transmitted-light intensity in state (1)
V_I, V_R	velocity of incident and reflected shocks
n	index of refraction in state (2)

TABLE 2. Measured properties.

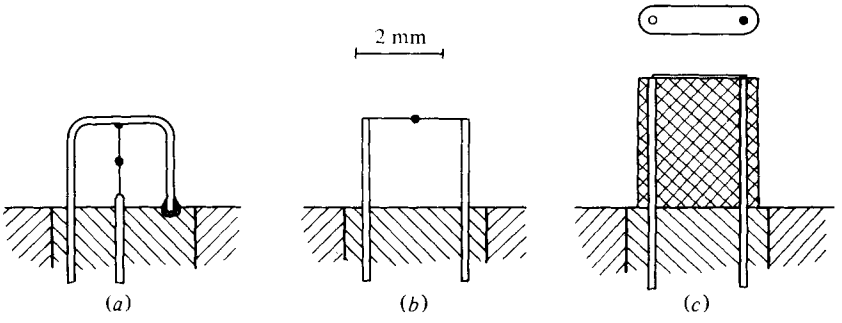

FIGURE 4. End-plate measuring elements. (*a*, *b*) Iron–constantan thermocouples. (*c*) Iron–constantan thermocouple for the measurement of the reflected-shock velocity V_R.

storage bottle. Diaphragm burst was effected in some experiments simply by continuously increasing the pressure P_D until the diaphragm burst spontaneously, in the other experiments by piercing the diaphragm with the spring-loaded arrowhead plunger. Following the diaphragm burst, the experimental events of interest were complete and recorded within about 10 ms. About three experimental runs (shots) per hour could be achieved.

Measured properties. Measured experimental variables are shown in table 2, all but the initial-state properties being measured in the observation section. Not all of the properties in table 2 were measured in any given run.

Transient pressures were measured by Kistler quartz piezoelectric transducers type 603B, membrane diameter 3·5 mm; Vibro-Meter type TA-3C charge amplifiers converted the piezoelectric charge to an output voltage signal. Transient temperatures were measured at transducer positions T12 and T13 with iron–constantan thermocouple elements designed to produce the fastest possible temperature response consistent with a lifetime of at least several shots. A proven element is shown in figure 4(*a*), an earlier version in figure 4(*b*). Both designs used wires tapered by etching until the small-end diameter was about 10 μm. The two ends were then welded together by means of a current pulse to form the thermocouple. The response time of the elements was more than 2 ms in air ($P \sim 5$ bar) and about 0·1 ms in the test liquids.

The transmitted-light intensity $I(t)$ behind the incident shock wave was measured at the transducer position $T1$. The beam from a helium–neon laser ($\lambda = 533$ nm, beam diameter 0·6–0·7 mm) was directed through the narrow side windows, perpendicular to the axis of the shock tube, onto a 2 mm diameter photodiode.

The velocity V_I of the incident shock wave was determined from the $P(t)$ signals from positions $T1$ and $T3$, and checked from time to time with the signals from $T1$, $T2$, $T3$ and $T13$. The velocity V_R of the reflected shock wave could not be determined by this

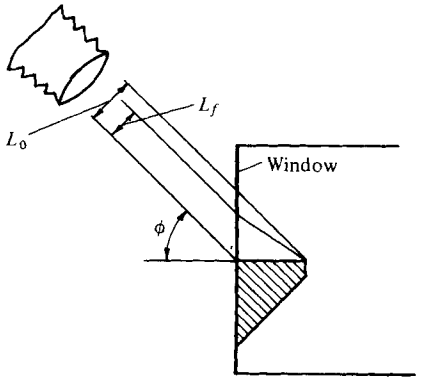

FIGURE 5. Measurement of the index of refraction n by the altered apparent length L on the face of an immersed wedge.

method because of the limited distance of travel and because of strong boundary-layer interactions ahead of the shock. Consequently, a special probe built for the measurement of V_R was mounted at position $T13$ as shown in figure 4(*c*). Passage of the incident and reflected shocks over the thermocouple layer at the end of this probe produced successive jumps in its output signal. Comparing the time of these jumps with the time at reflexion, as indicated by the jump in the output signal of the pressure transducer mounted at position $T12$, allowed the determination of the velocity V_R (and, with considerably less accuracy, of V_I).

The index of refraction n of the fluid in state (2) was measured photographically according to the altered apparent length of an immersed object, as shown schematically in figure 5. The value of n follows from the elementary formula

$$n^2 - 1 = (a^2 - 1)\cos^2\phi, \tag{1}$$

where $a = L_0/L_f$. This measurement was made in relatively few experiments.

All of the time-dependent variable output signals (P, T, I) were stored in four transient recorders Datalab type DL 905, each recorder having a $2^8 \times 2^{10}$-bit $y-t$ capacity. The recorder $y(t)$ data were then plotted via an analog-digital converter with a y, t plotter. Certain data were displayed on a storage oscilloscope.

Photographic apparatus. Various forms of photography were used in the observation section. Photographs were mainly conventional, the visibility of the image depending on the presence of phase boundaries, as in the case of liquid droplets in a gas.

Rolleiflex SL 66 cameras with 6 × 6 cm film format were used for individual pictures. In a few experiments two cameras were arranged to make stereoscopic pictures. In every case, two General Radio Strobotac flash lamps were used for illumination, the flash being triggered through a variable time delay from a pressure transducer at $T1$, $T2$ or $T3$. The time of flash exposure was registered in a transient recorder from a photodiode signal.

Motion pictures were made with a Fastax 16 mm camera (maximum framing rate $\sim 8500\,\mathrm{s}^{-1}$) and two Variolux light sources. Synchronization between camera and experiment was provided by initiating the plunger-actuated diaphragm burst from a camera output signal which was automatically triggered after the camera start.

In all the photographic and optical observations, insulating covers remained over the windows until about 30 s before diaphragm burst.

3. Thermodynamic model

The property calculations used for comparison with and conversion of experimental data are based on the 'BWR 44' equation of state (denoting a Benedict–Webb–Rubin equation with 44 constants) of Yamada (1973) and were checked in some cases using the virial-type equation of Hobbs (1976). The calculation of property jumps across a shock flow from conventional shock theory with assumed equilibrium states upstream and downstream of the shock (in certain cases, with assumed metastable states, i.e. supersaturated vapour) was performed as described by Thompson & Sullivan.

In view of the stated aim to establish the existence of liquefaction, it is well to keep in mind what a 'liquid' is. According to the conventional thermodynamic definition, a liquid is the disordered homogeneous phase which exists at temperatures less than the critical and densities greater than the critical:

$$T \leqslant T_c, \quad \rho \geqslant \rho_c.$$

These conditions will be satisfied for a homogeneous phase if the pressure exceeds the saturation pressure $P_s(T)$:

$$T \leqslant T_c, \quad P > P_s(T).$$

The critical properties P_c, ρ_c and T_c of the experimental substance serve as essential reference points for these conditions and will be indicated in the figures showing experimental results.

4. Experimental results for partial liquefaction shocks

Condensation behind the incident shock **I** was studied. In these experiments, the upstream state (0) consisted of superheated gas and the equilibrium downstream state (1) varied from superheated gas to a gas–liquid mixture, with a maximum of 10% moisture. The extent of liquefaction was thus minimal, with an expected downstream state consisting of liquid droplets in gas. The test substance was PP3 in every case: the three different sets of initial conditions used are shown in the first three rows of table 4.

In order to get some idea of the uniformity of the incident shock behaviour, its position was recorded as a function of time at four different pressure-transducer locations. The average shock Mach number was determined for each pair of transducer locations, based on the difference in arrival time: the result is shown in figure 6. At the highest Mach number shown, spontaneous condensation was observed in state (1) behind the incident shock.

The effect of increasing the Mach number M_I of the incident shock is to bring the shocked state (1) nearer to the saturation boundary and then into the mixture region, where spontaneous condensation is to be expected. Before a saturated state (1) is reached, however, condensation is observed in the boundary layer in the form of a thin layer of fog near the wall. Considering that the wall temperature remains close to the initial temperature T_0 throughout the experiment, the layer of fluid immediately adjacent to the wall undergoes nearly isothermal compression and thus, with increasing M_I, reaches saturation well before the bulk fluid in state (1): this situation is shown diagrammatically in figure 7 (*a*). The thickness of the fog layer was measured by directing and flashing a collimated light beam at location $T1$ through one of the side

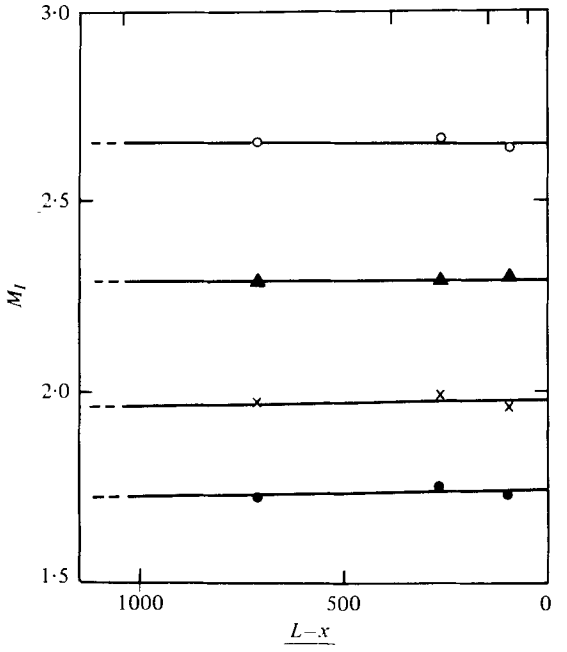

FIGURE 6. Incident-shock Mach number M_I as a function of distance $L-x$ from the test-section end wall. Initial state: $T_0 = 130$ °C, $P_0 = 0{\cdot}67$ bar.

windows. A bright column was formed by scattering where the beam passed through the fog layer: the height h of the column was then measured photographically through the rear window. By flashing the light source with a measured delay from the time of arrival of the incident shock, and making use of the measured shock velocity, the distance d behind the shock corresponding to the measured height h could be determined. Results are shown in figure 7 (*b*).

The thickness δ of the momentum boundary layer has been estimated for comparison with the thickness h of the fog layer. The Reynolds number du_1/ν reaches a value of 10^6 at a distance $d \sim 3$ mm behind the shock: the boundary layer can thus be considered turbulent over its length for this purpose. The expression of Mirels (1971) is

$$\delta \sim d^{\frac{4}{5}}(\nu_w/u_1)^{\frac{1}{5}}, \tag{2}$$

where $\nu_w \equiv \mu_w/\rho_w$ is the kinematic viscosity at the wall conditions (P_1, T_0) behind the shock and u_1 is the bulk fluid velocity behind the shock. The value of $\delta(d)$ from (2) is plotted in figure 7 (*b*) for the case $M_I = 2{\cdot}4$. Because this value increases with decreasing Mach number, the predicted δ is greater for the case $M_I = 2{\cdot}2$, that is, the fog layer is much thinner than the boundary layer. Bearing in mind that the thermal boundary layer is necessarily similar to the momentum boundary layer, this would be expected, since the bulk fluid is well above the saturation temperature in this case. These results appear to be consistent with the light-extinction measurements discussed below.

Light transmission measurements and the onset of spontaneous condensation. As described in § 2, measurements of the transmitted light intensity $I(t)$ behind the incident shock were made for a laser-light beam traversing the shock tube. A sample $I(t)$ trace, with the corresponding pressure records, is shown in figure 8. The sudden dip in

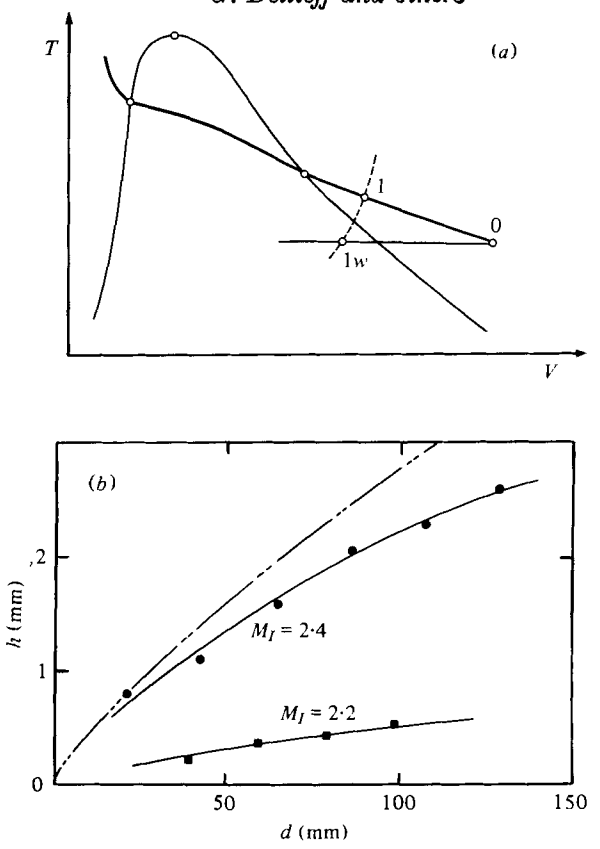

FIGURE 7. Formation of a boundary fog layer. (*a*) Temperature–volume diagram illustrating a supersaturated state (1*w*) at the wall with a superheated state (1) behind the incident shock. Heavy line is the shock adiabat, light line the isotherm $T = T_0$, dashed line the isobar $P = P_1$. (*b*) Thickness h of the layer as a function of the distance d behind the incident shock, $T_0 = 130$ °C, $P_0 = 0{\cdot}67$ bar. Solid lines are drawn through the measured data points for the fog layer; the dashed line shows the estimated boundary-layer thickness for $M_I = 2{\cdot}4$ as described in the text.

intensity at the time of arrival of the shock can be interpreted as a deflexion of the light beam by the shockfront; the following overshoot in intensity can be interpreted as an increase in the transmission coefficient at the glass–fluid boundary due to the increase in the index of refraction in the fluid across the shock. All of the measured intensities, when plotted semilogarithmically against time, yielded approximately straight lines, with the corresponding form for $I(t)$

$$I/I_0 = e^{-\beta t}. \tag{3}$$

The value of the decay constant β is plotted against M_I for the three different initial states in figure 9. The initial straight-line segment in each of the $\beta(M_I)$ curves, starting from $\beta = 0$, is interpreted as light attenuation (scattering) due exclusively to the boundary fog layer, consistent with the already-mentioned optical observations of that layer. The discontinuity in the slope of $\beta(M_I)$ is interpreted as the onset of spontaneous condensation in the core flow. For comparison, the vertical lines in figure 9 show the predicted Mach number M_I for the onset of condensation from the thermodynamic model described in §3.

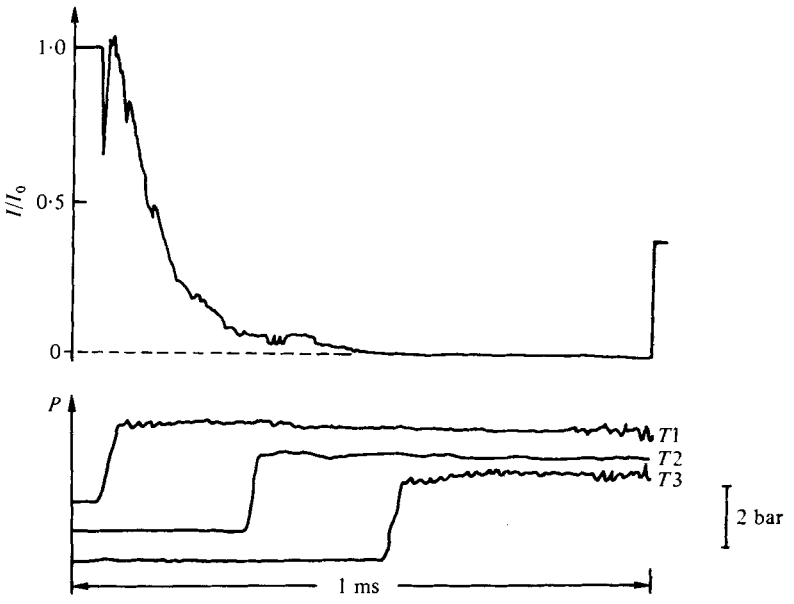

FIGURE 8. Measured transmitted light intensity I and pressure P ahead of and behind the incident shock as functions of time. Initial state: T_0 = 130 °C, P_0 = 0·67 bar. Shock Mach number M_I = 2·28.

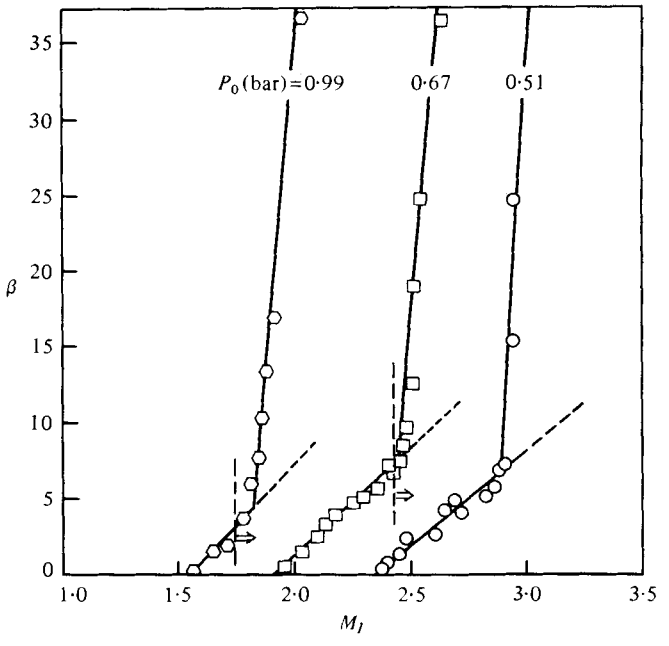

FIGURE 9. Measured decay constant β, defined by equation (2), as a function of the incident shock Mach number M_I.

M_I	ρ_k (kg m^{-3})	%	$r \times 10^6$ (m)	$N \times 10^{-17}$ (m^{-3})	Δ (mm)
2·5	1·63	2·7	8·1	6·3	20
2·6	3·26	5·0	8·7	10·5	10
2·7	5·57	7·9	9·2	15·1	5

TABLE 3

Estimates of the condensation history behind the incident shock. Based on the idea that the decay constant β in (3) can be expressed as the sum $\beta_{bl}+\beta_{cf}$ of a boundary-layer and a core-flow contribution, Speckmann (1978) has estimated the droplet size behind the shock. The model implied by (3) is that of an attenuation coefficient α which increases from zero linearly with time, without ever reaching an upper limit: in conjunction with an assumed Rayleigh light-scattering model (see e.g. Born 1972; Kerker 1969), valid for $\lambda \gg r$, this yields for the droplet number density N and droplet radius r,

$$Nr^6 = kt, \tag{4}$$

where the constant of proportionality k depends on the value β_{cf} determined from figure 9. Equation (4) is clearly incorrect for large times, since it predicts that the mass density of condensate $\rho_k \sim Nr^3$ grows without limit. This corresponds to the absence of a finite lower bound for $I(t)$ in (3), reflecting the inability to measure small light intensities with the measuring device employed. If, however, one assumes that (4) holds up until some large time t_1 at which condensation is complete, with the density of condensate ρ_k predicted by the thermodynamic model, then (4) together with mass conservation can be used to predict numerical values for N and r. Arbitrarily setting t_L to 0·5 ms yields the estimates shown in table 3, for an initial state $t_0 = 130\,^\circ$C and $P_0 = 0{\cdot}67$ bar. In table 3, the third column indicated the mass per cent of condensate in state (1). The quantity Δ, intended as a crude measure of the thickness of the condensation zone, shows the distance downstream of the shockfront at which the transmitted light intensity has fallen to 10 % of its maximum value. These results are in fair agreement with detailed calculations of nucleation and droplet growth (M. Bratos 1978, private communication).

Quite aside from the limitations of the measurements and models described, it should be borne in mind that these estimates apply to the feeble end of the liquefaction shock spectrum. It may be expected that the structure of a complete liquefaction shock is qualitatively different.

5. Experimental results for complete liquefaction shocks

Complete liquefaction behind the reflected shock **R** was studied. In order to show the transitions, with increasing Mach number M_I, from a single-phase gas → gas shock to a gas → mixture shock to a gas → liquid shock, measurements over a corresponding range of 'shock strength' M_I will be reported. The emphasis, however, is on the experimental confirmation of the existence of a complete liquefaction shock, that is, a shock transition from superheated gas (1) to compressed liquid (2).

The various test fluids and the corresponding initial states used are shown in table 4. More than 80 % of the runs were made with the substance PP3.

Substance	T_0 (°C)	P_0 (bar)	m_0 (g)
PP3	130	0·51	73
	130	0·67	99
	130	0·99	149
PP3	80	0·24	38
PP9	130	0·24	43
FC40	150	0·33	73

TABLE 4. Fluids and initial states.

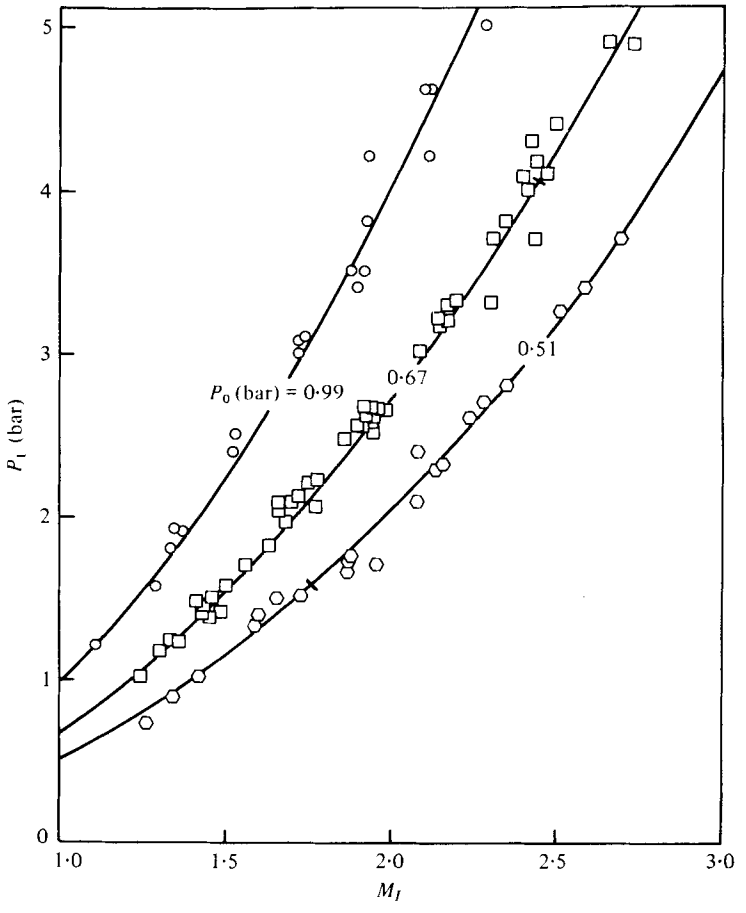

FIGURE 10. Pressure P_1 downstream of the incident shock and upstream of the reflected shock as a function of incident-shock Mach number M_I in PP3. Solid curves represent the calculations. Transverse marks on the curve indicate the onset of spontaneous condensation in state (1). Data: ○ , P_0 = 0·51 bar; □, P_0 = 0·67 bar; ○, P_0 = 0·99 bar.

For purposes of the liquefaction shock experiment, the incident shock should bring the test gas to a slightly superheated (dry) state (1) in motion towards the shock-tube end wall. Such a state is indicated in table 5, which shows a typical sequence of states for the case of complete liquefaction: the properties shown for states (1, 2) are calculated properties. A comparison of the measured pressures P_1 behind the incident shock with

State	P (bar)	T (°C)	T_{sat} (°C)	ρ (kg m^{-3})	c (m s^{-1})	u (m s^{-1})	M_S
0	0·67	130	90	8·33	89·3	0	
							2·43
1	4·02	158	155	55·6	88·2	185	
							2·19
2	24·0	229	—	1190	—	0	

TABLE 5. Typical sequence of states (PP3).

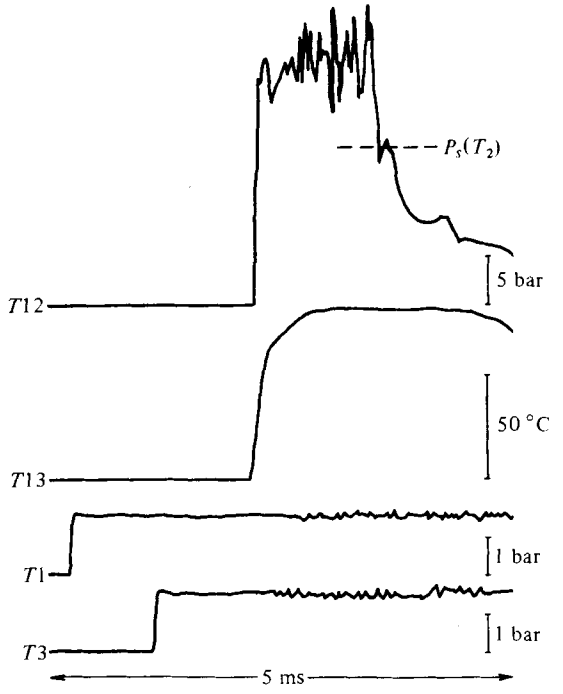

FIGURE 11. Pressure and temperature histories with complete liquefaction. The pressure P_2 and temperature T_2 are indicated by T12 and T13 respectively. T1 and T3 show the pressure outside of the liquefaction shock region. PP3, T_0 = 130 °C, P_0 = 0·67 bar, M_I = 2·40.

the calculated values is shown in figure 10. For sufficiently large shock Mach numbers M_I, the state (1) becomes wet, as discussed in §4 and shown in the figure. The onset of condensation in state (1) is not manifested in the pressure measurements themselves.

Directly measured properties. The pressure P_2 and temperature T_2 were measured at positions $T12$ and $T13$, respectively, in figure 3. Representative pressure–temperature histories are shown in figures 11 and 12. The arrival of the incident shock at the end wall is signalled by the abrupt rise in the signals $T12$ and $T13$. There follows a plateau, indicating the state (2) behind the reflected liquefaction shock: the length of this pressure plateau corresponds approximately to the time duration of the liquefaction-shock phenomenon. The arrival of the contact surface (and corresponding fall of the inflowing momentum, because the density $\rho_5 \ll \rho_1$) is then signalled by a rapid fall in the pressure, temporarily interrupted at the saturation-pressure level.

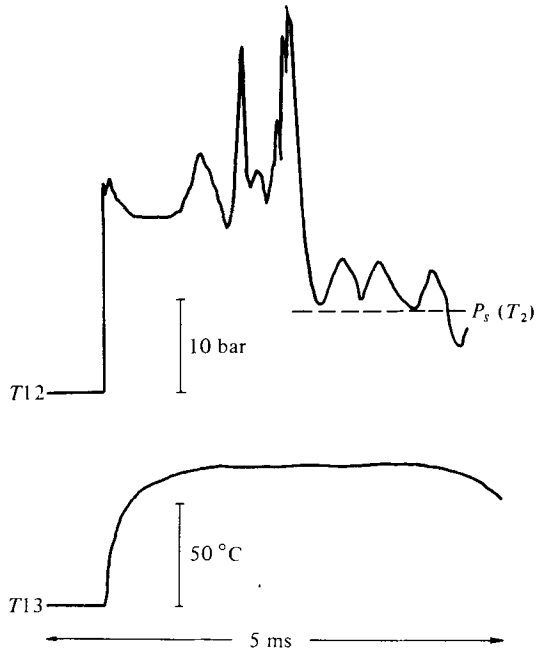

FIGURE 12. Pressure and temperature histories with complete liquefaction. PP3, T_0 = 130 °C, P_0 = 0·99 bar, M_I = 1·95.

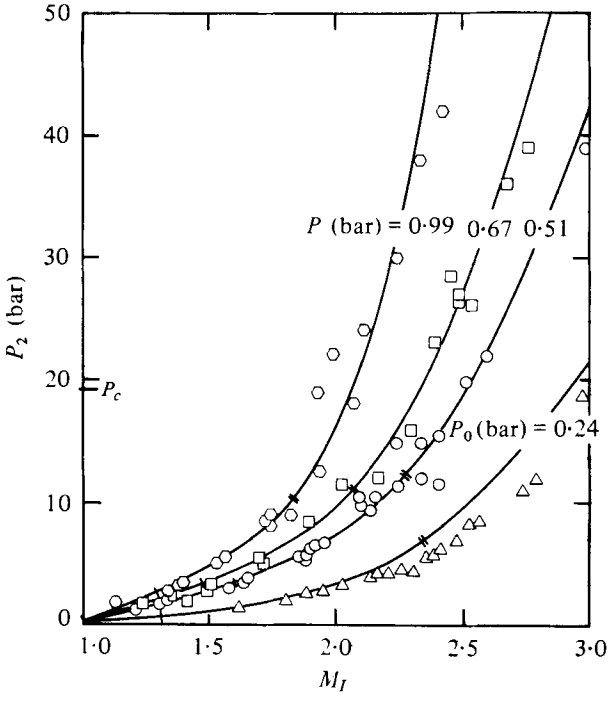

FIGURE 13. Pressure P_2 downstream of the liquefaction shock as a function of incident-shock Mach number M_I in PP3. Solid curves represent calculations, with transverse marks indicating the calculated onset of condensation and of complete liquefaction. Data: △, P_0 = 0·24 bar; ○, P_0 = 0·51 bar; □, P_0 = 0·67 bar; ○ , P_0 = 0·99 bar.

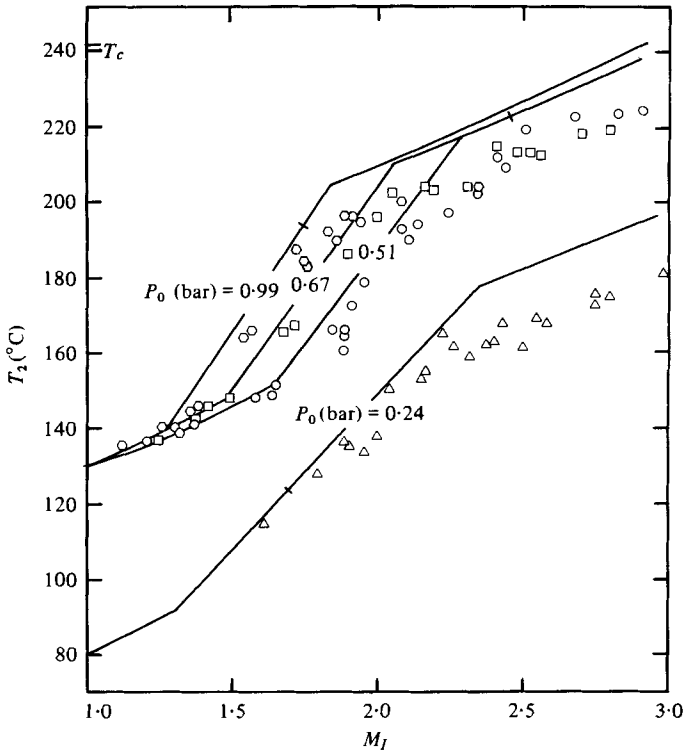

FIGURE 14. Temperature T_2 downstream of the liquefaction shock as a function of incident-shock Mach number M_I in PP3. Solid curves represent calculations; the points of discontinuity in slope represent the onset of condensation and of complete liquefaction. Transverse marks indicate the onset of condensation in state (1). Data symbols are as in figure 13.

Large-amplitude oscillations in the pressure P_2 are observed. It is probable that the oscillations in figure 11 are due to ringing of the observation section: a similar oscillation, which has nearly the same frequency and propagates away from the end wall with a definite velocity, is seen in the signals $T1$ and $T3$ from the side-wall transducers. The large-amplitude pressure peaks near the end of the liquefaction plateau seen in figure 12 were characteristic of early experiments.

The measured pressures P_2 for all of the PP3 experiments are plotted as a function of the incident-shock Mach number in figure 13. The pressures shown were determined as the mean pressure of the plateau, discounting systematic peaks such as those at the end of the plateau in figure 12.

The agreement between the measured and predicted pressures in figure 13 is reasonably good, but there is no vivid indication of the onset of condensation and, at a larger Mach number M_I, of complete liquefaction. The measured temperatures T_2 are more satisfactory in this respect, as shown in figure 14. For any given set of initial conditions, each calculated curve has a distorted, angular S-form: the lower and upper bars of the 'S' correspond to states (2) in the dry vapour and compressed liquid states, respectively, and the steep diagonal corresponds to liquid–vapour mixture states. The vertical separation ΔT between the upper and lower bars is a rough measure of the latent heat $L \sim c_p \Delta T$. The sequence of experimental data points is geometrically

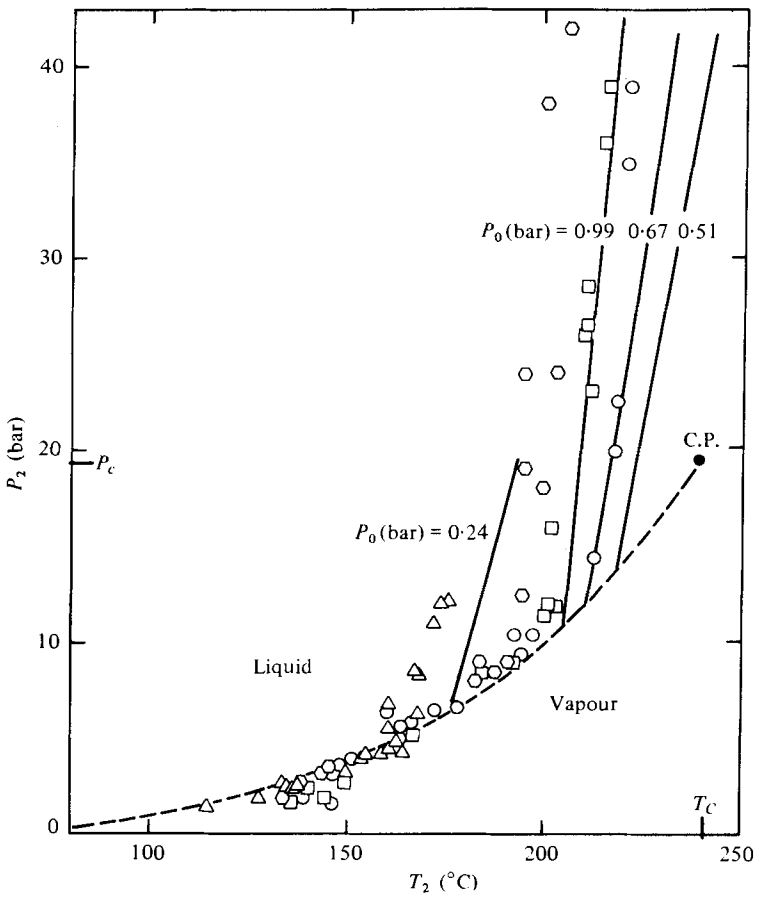

FIGURE 15. Pressure P_2 *versus* temperature T_2 downstream of the liquefaction shock in PP3. Calculated results lie on the dashed vapour-pressure curve and on the solid lines. Data symbols are as in figure 13.

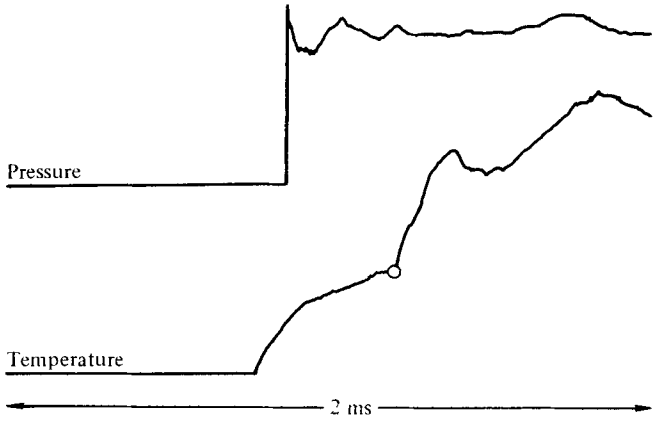

FIGURE 16. Output temperature signal from the thermocouple probe designed to measure the reflected shock velocity V_R, with the simultaneous end-wall pressure signal used to establish the time of arrival of the incident shock. PP3, P_0 = 0·67 bar, T_0 = 130 °C, M_I = 1·78. The small circle on the T trace indicates the arrival of the reflected liquefaction shock.

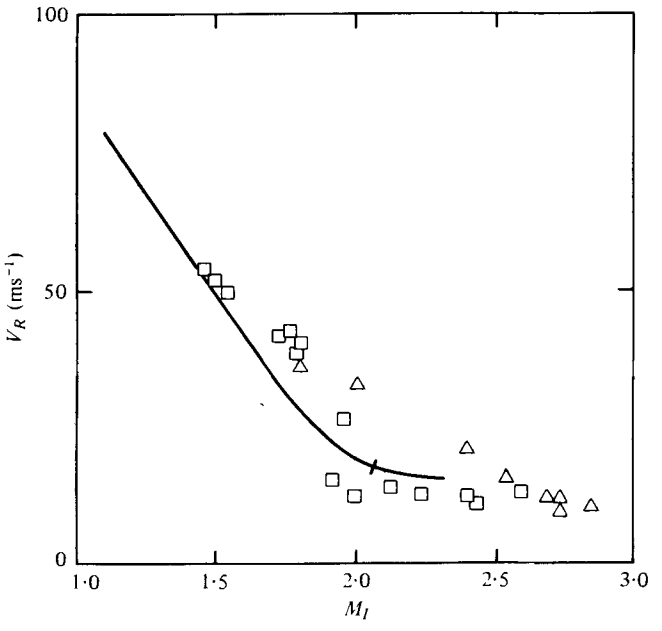

FIGURE 17. Reflected liquefaction shock velocity V_R as a function of incident Mach number M_I in PP3. The solid curve shows the calculated result for $P_0 = 0{\cdot}67$ bar, $T_0 = 130$ °C, with a transverse mark indicating the onset of complete liquefaction. Data symbols are as in figure 13.

similar to the calculated 'S' curve. The existence of complete liquefaction states along the upper bar of the 'S' thus appears to be experimentally verified, but with a deviation (~ 10 °C) from the predicted end temperature T_2.

We cannot offer a definitive explanation for this deviation. It seems likely that it is due mainly to inaccuracies in the (estimated) material properties of the test substance: the essential parameter L/c_p depends on the slope of the vapour-pressure curve and the volume change on evaporation (via the Clapeyron equation) and on the heat capacity, all of which are inaccurately known. A further inaccuracy lies in the equation of state, which is not accurate at high densities. It is, in any case, considered unlikely that the large temperature deviation is attributable to measurement error or to non-equilibrium effects.

The achievement of measured complete-liquefaction end states is indicated clearly in figure 15. By definition, the compressed-liquid states lie above the vapour-pressure curve and to the left of a vertical line $T = T_c = \text{constant}$.

The velocity of the reflected liquefaction shock was measured with the probe already described (figure 4*c*). A sample output trace from the probe is shown in figure 16. The resulting velocities are shown in figure 17, and confirm the theoretical prediction fairly well.

Index of refraction n_2 was measured behind the liquefaction shock as described in §2.

Determination of the density ρ_2. Indirect measurements of the density ρ_2 behind the liquefaction shock were made in three (nearly) independent ways.

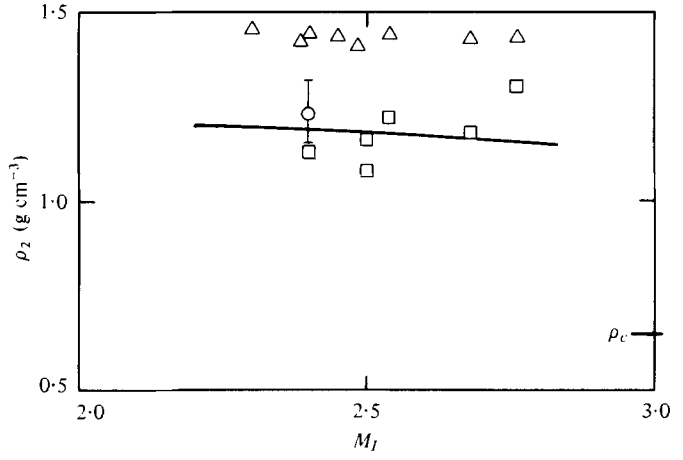

FIGURE 18. Liquid density ρ_2 as a function of incident shock Mach number M_I in PP3. □, from measured shock velocity, equation (5); ○, from measured index of refraction, equation (6); △, from equation of state with measured P_2, T_2; ——, theoretical prediction.

The first method uses the measured shock velocity V_R in conjunction with the continuity condition across the shock, which yields

$$\rho_2 = \rho_1(u_1/V_R + 1), \tag{5}$$

where ρ_1 and u_1 can be calculated from the measured properties M_I, P_0 and T_0.

The second method uses the measured index of refraction n_2 in conjunction with the Lorenz–Lorentz equation

$$k_{\mathrm{LL}} = \frac{n^2-1}{n^2+2}\frac{1}{\rho}. \tag{6}$$

The Lorenz–Lorentz parameter k_{LL} is nearly constant for non-polar fluids, with deviations of the order of one per cent (for an explicit treatment, see Olson 1975). To this approximation, k_{LL} can be taken as a material constant which can be found from a simultaneous determination of the density ρ and refractive index n. For the test substance PP3, the saturated-liquid density $\rho = 1{\cdot}840$ g cm^{-3} at 20 °C with a corresponding index of refraction 1·28 yields the value $k_{\mathrm{LL}} = 38{\cdot}14$ cm^3 mol^{-1} (this 'average' value was determined with the same Strobotac white-light flash source used in the shock-tube experiments).

The third method uses the thermal equation of state to calculate $\rho(P_2, T_2)$ from the measured pressure and temperature.

The three distinct experimental determinations of density are compared with the theoretical curve in figure 18. The dispersion is very large, but all methods yield density values within the liquid region.

Photographic observations. Using the equipment described in §2, conventional photographs and motion-picture films were made through the circular end window. The various lighting and camera arrangements are shown in figure 19.

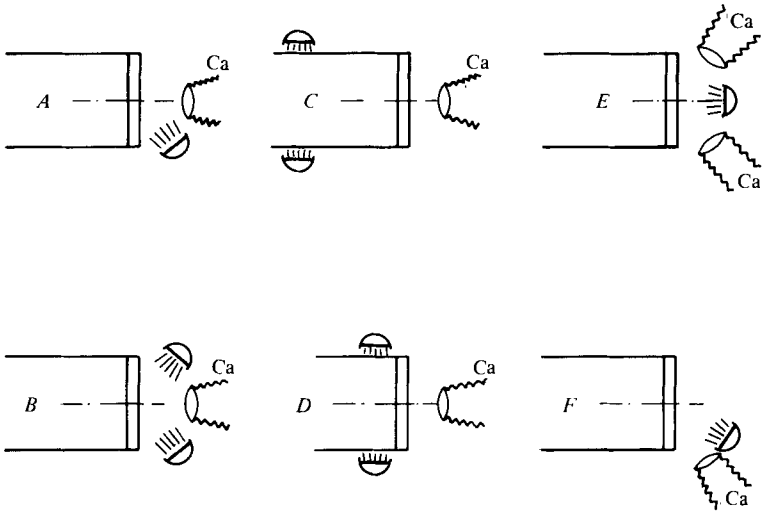

FIGURE 19. Schematic diagrams of the various lighting/camera arrangements used for photography. Ca designates the camera location.

The most important photographically observed results can be summarized as follows:

(i) A clear phase, interpreted as a liquid, is observed in region (2).

(ii) Torus-form two-phase objects (rings) appear in region (2) and appear to be formed within or immediately behind the liquefaction shock.

(iii) The shock-tube boundary-layer vorticity in the test gas becomes concentrated in a large ring, interpreted as a vortex, surrounding region (2) at the end of the shock tube. This corner vortex is the dominant visible structure in the shock–boundary-layer interaction.

(iv) In the terminal phase of the liquefaction, a small ring (ii) is naturally selected and grows rapidly on the shock-tube axis until it meets the growing corner vortex (iii).

(v) The region which includes the shockfront and the phase transition, roughly designated as the shockfront, varies in appearance from smooth to rough and feathery, depending on the substance and experimental conditions.

These results are described in more detail in the following. A sequence of motion-picture frames, showing the entire liquefaction history, is shown in figure 20 (plates 1 and 2). Frame 1 corresponds to a time shortly before the arrival of the incident shock: the absence of any backscattered light, i.e. of a visible fog, is characteristic of a dry or supersaturated state (1). The incident shock is reflected between frames 1 and 2. Small rings described in (ii) above can already be seen in frame 2: some are observed to grow with time. The large corner vortex described in (iii) above can be seen in frame 5 and becomes larger thereafter (note that the inside frame diameter of 70 mm is smaller than the shock-tube inner diameter 80 mm). In frame 8 a ring near the shock-tube axis has been selected and thereafter grows rapidly until it meets the corner vortex ring (frames 8–11). In frame 12, liquid is no longer visible. The arrival of the contact-region between driver gas and test gas is placed between frames 11 and 12, based on the pressure record in figure 11.

In the following plates, t_R designates the time after the arrival of the incident shock.

The appearance of the small torus-form rings behind the liquefaction shock was unexpected. There are several reasons for believing that these rings are, in fact, *vortex rings*. This hypothesis is supported by the following qualitative arguments.

(i) The visual impression is that of a torus, rather than, for example, that of a spheroidal 'droplet' or 'bubble'. This impression is especially strong in the stereoscopic photographs.

(ii) The ring-vortex form with a visible two-phase core is consistent with the dynamical pressure distribution in a ring vortex.

(iii) The observed flow patterns and inferred growth and decay of the rings are similar to those found in ring-vortex experiments. In particular, a period of initial growth and ring fusion followed by wave-form instability and subsequent decay is observed.

These effects can be seen in figures 20–23. Figure 21 (plates 3 and 4) conveys a visual impression of the rings under three different conditions of illumination. Figure 22 (plate 5) shows rings at an early and at a mature stage of development. The vortex rings found in our experiments are believed to originate as small rings ($d < 60\,\mu$m) in or immediately behind the liquefaction shock, and to grow, fuse and then decay as they move away from the shockfront, such that a few rings survive to full-grown maturity ($d \sim 4$ mm). Vortex-ring growth was verified by multiple-exposure photography. Many cases of apparent fusion, as described for ring vortices by Oshima & Osaka (1975), can be seen in figure 22(*a*); decay, including a few cases of apparent wave-form instability, as described for example by Liess & Didden (1975) and by Maxworthy (1977), can be seen in figure 22(*b*).

Various photographs not reproduced here indicate that the creation of very small rings in or near the shockfront is a process which continues throughout the lifetime of the shock.

A rough estimate of the vortex-ring strength can be based on the idea that the visible outer boundary of the ring is near the vapour pressure of the fluid in state (2), at least in the early part of the life of the ring. Assuming steady inviscid flow external to this boundary (i.e. outside the visible ring) yields for the tangential velocity u_b at the boundary

$$u_b^2 \sim 2(P_2 - P_{\mathrm{sat}})/\rho_2, \tag{7}$$

where P_{sat} can be estimated as the saturation pressure at T_2. For the range of pressure differences $P_2 - P_{\mathrm{sat}}$ from 2 to 32 bars (see e.g. figure 15), this yields values of u_b in the range from 20 to 80 m s^{-1}; for a core diameter of 40 μm, the larger velocity yields a vortex ring circulation $\Gamma \sim 10^{-2}\,\mathrm{m^2\,s^{-1}}$, somewhat greater than that of a smoker's smoke ring. The assumptions here are tenuous and this estimate should be used with caution.

The three-dimensional arrangement of rings behind the shock can be seen in the stereoscopic pictures in figure 23 (plate 6) (some individuals have the ability to view these pictures as a single three-dimensional image, from a distance $\sim$ 10 cm with the eye relaxed; otherwise, some type of viewing device is necessary). The larger rings are clearly seen to lie well above a background of small rings.

It was found that the ring objects could be artificially produced by cementing small obstacles onto the inside surface of the end window. For example, a thin wire bent into a V-form and fastened with the sharp vertex of the V pointing towads the diaphragm of the shock tube produced repeatable rings centred on the vertex.

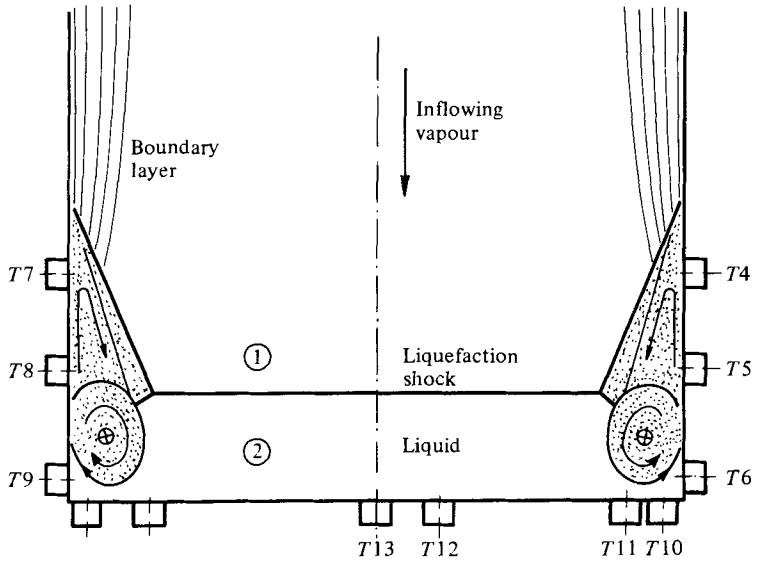

FIGURE 25. Inferred structure of the shock–boundary-layer interaction region under conditions of complete liquefaction.

Three pictures of the shockfront under various experimental conditions are shown in figure 24 (plates 7 and 8). The L-shaped template in figure 24(*a*) was cemented to the inside surface of the window, in order to gain a rough visual impression of the shock 'surface' by projecting a shadow onto it. The upper and lower arcs seen in figure 24(*b*) are unexplained. In figure 24(*c*), the visible structure has become rough and feathery, this effect tending to increase with increasing moisture content y in state (1), upstream of the shockwave. The feathery 'front' in this case appears to run ahead of the shockwave.

Shock–boundary-layer interaction region. The interaction of the shock-tube boundary layer and the reflected liquefaction shock produce a complicated three-dimensional flow. Interaction flows of this kind are already familiar for reflected shocks in gases, where the thickness of the interaction region is found to increase with decreasing ratio of specific heats γ, as discussed by Davies & Wilson (1968) and by Honda *et al.* (1975). This behaviour can be associated with the large density jump across the shock (for $\gamma \rightarrow 1$) and is thus consistent with the enhanced interaction effects found in our experiments.

A schematic reconstruction of the interaction flow is shown in figure 25. The main liquefaction shock divides into two branches near the wall, forming the 'λ-shock' or 'bifurcation'. One oblique-shock branch extends far upstream. Vapour from region (1) is compressed by this shock into a wedge-shape region as an opaque two-phase mixture: the outflowing mixture is assumed to roll up into the corner vortex. As pointed out by a reviewer, an outward radial flow would be consistent with the presence of the corner vortex and its image in the end wall. The direction of any such radial flow could not be established on the basis of the experiments, however. A recirculation region or 'separation bubble' lies upstream of the corner vortex, geometrically consistent with the flow deflexion of the leading oblique shock.

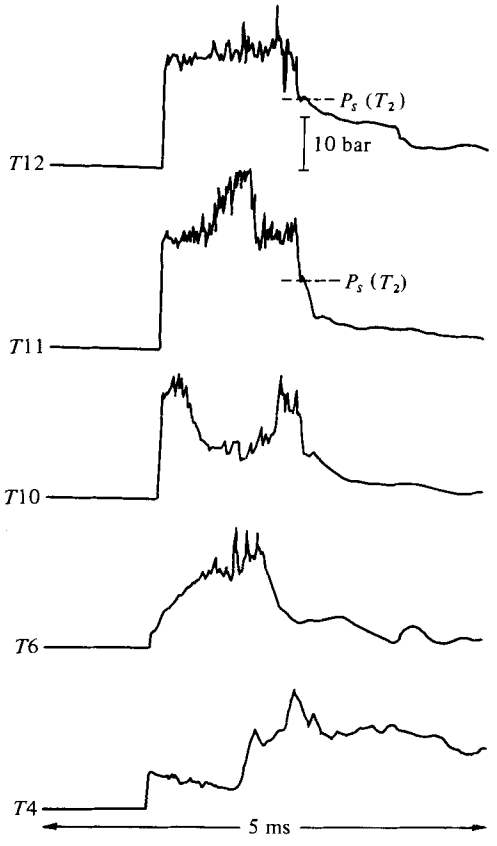

FIGURE 27. Pressure histories near the shock-tube end wall during the liquefaction. PP3, T_0 = 130 °C, P_0 = 0·67 bar, M_I = 2·4. For transducer locations, see figures 3 and 25.

A photograph of the ring-shaped region referred to here as the corner vortex is shown in figure 26 (plate 9). It is convenient to think of this vortex as the captive counterpart of the well-known vortex ring expelled from the open end of a shock tube, following an outgoing incident shock (Elder & de Haas 1952), which is in turn basically similar to the ring produced by a conventional vortex generator (e.g. Maxworthy 1977).

The pressure distribution on the wall near the end of the observation section is non-uniform, corresponding to the three-dimensional interaction flow. Pressure histories are shown in figure 27. The approaching incident shock is first registered by transducer trace $T4$, which also shows the arrival of the upstream branch of the reflected shock. The falling pressure following the arrival of the incident shock here is *not* observed in the upstream transducer trace $T3$ (see figure 11), but is observed at positions $T5$ and $T8$. Interchanging the pressure transducers (with amplifiers), for example between positions $T3$ and $T5$, did not alter this result. The pressure distribution near the end wall is almost axially symmetric, as indicated by comparative traces from symmetrically placed transducers (not shown). The traces from transducers $T11$ and $T12$ show an approximately uniform pressure distribution in the neighbourhood of the shock-tube axis, consistent with a one-dimensional flow model for this region. On the basis of

continuity, however, a low-speed inward displacement of liquid would be expected during the liquefaction phase, leading to a reflected-shock velocity V_R somewhat greater than that predicted by a one-dimensional model.

6. Concluding remarks

It appears that the liquefaction shock wave does exist in a form consistent with classical shock-wave theory.

The variety of associated phenomena found in our experiments was not anticipated, nor has each one been thoroughly investigated. The existence of the small shock-associated ring vortices, in particular, has been inferred rather than proven (in fairness, it should be mentioned that an earlier identification of these objects as 'bubbles' met with little objection!).

Accepting the plausibility of this inference, one naturally seeks a mechanism for the generation of the vortices in or behind the shockfront: is the liquefaction shock wave perhaps unstable? Instabilities leading to non-uniform flows behind the discontinuity have been observed in detonations (White 1961) and in ionizing shock waves (Meier & Sandeman 1975; Glass & Liu 1978). A theoretical basis for instability in the present case is not clear. The possibility of *shock splitting*, associated with the discontinuity in slope of the isentrope at the saturated-vapour boundary and first suggested by Bethe (1942), falls outside the range of the experiments reported here (see also Thompson & Sullivan 1975), nor was it observed.

A simple physical argument given by Y. B. Zel'dovich suggests a basis for non-uniform flow. The shock is not a true discontinuity and must have some small-scale internal structure. There is, however, no continuous sequence of homogeneous thermodynamic states connecting the equilibrium end state (1) and (2), as there would be for gaseous argon, for example (the absence of a continuous sequence of states is associated with the region of thermodynamic instability in which $(\partial P/\partial v)_T > 0$). Thus, states (1) and (2) are connected by discontinuous states similar to dropwise condensation.

The resulting situation of large density differences in a region of strong pressure gradient (deceleration) and condensation may well be unstable. Formation of a locally dense region – effectively, a droplet – would lead to the formation of vortices under the action of the shock pressure gradient, as predicted by the vorticity-growth equation

$$\rho \frac{D}{Dt}(\boldsymbol{\omega}/\rho) = \left(\frac{\boldsymbol{\omega}}{\rho}.\nabla\right)\mathbf{u} - \frac{\nabla P \times \nabla \rho}{\rho^2}, \tag{8}$$

where $\boldsymbol{\omega} \equiv \nabla \times \mathbf{u}$ is the vorticity and viscous terms are omitted for clarity. This is qualitatively similar to the vortex formation observed when a liquid drop falls onto a liquid free surface. A rough order-of-magnitude estimate from (8) of the resulting vortex-ring circulation yields a result of the same order as that previously found from velocity estimates. The vortex thus developed has a flow through its centre directed towards the end wall: this sense of rotation is consistent with the amplification of an initially small vortex near the shock-tube centre-line, induced by the flow field of the corner vortex, as displayed so strikingly in figure 20. The entire question of shock structure, possible droplet formation and vortex formation remains to be investigated.

We should like to express our gratitude to D. A. Sullivan for programming the theoretical calculations and to H.-G. Wagner for the donation of the original shock tube. Several scientists and technicians at the Max-Planck-Institut für Strömungsforschung and B. V. L. Trazomidrev of AREPO Ltd provided valuable support. Thanks are also due to reviewer B, whose suggestions for discussion of the ring-vortex hypothesis have been incorporated into this paper.

REFERENCES

BETHE, H. A. 1942 The theory of shock waves for an arbitrary equation of state. *Office Sci. Res. and Dev., Washington, Rep.* no. 545, p. 57.

BLYTHE, P. A. & SHIH, C. J. 1976 Condensation shocks in nozzle flows. *J. Fluid Mech.* **76**, 593–621.

BORN, M. 1972 *Optik.* Springer.

DAVIES, L. & WILSON, J. L. 1968 The influence of shock and boundary layer interaction on shock tube flows. In *Proc. 6th Int. Shock Tube Symp.*, Ernst-Mach-Inst., Freiburg i. B.

DETTLEFF, G. 1978 Experimente zum Nachweis der Verflüssigungsstoßwelle in retrograden Gasen. Dissertation, Georg-August-Universität Göttingen.

DETTLEFF, G., THOMPSON, P. A. & MEIER, G. E. A. 1976 Initial experimental results for liquefaction shock waves in organic fluids. *Arch. Mech.* **28**, 827–836.

ELDER, F. K. & DE HAAS, N. 1952 Experimental study of the formation of a vortex ring at the open end of a cylindrical shock tube. *J. Appl. Phys.* **23**, 1065–1069.

GLASS, I. I. & LIU, W. S. 1978 Effects of hydrogen impurities on shock structure and stability in ionizing monatomic gases: Part 1, argon. *J. Fluid Mech.* **84**, 55–77.

HOBBS, D. E. 1976 Unpublished.

HOMER, J. B. 1971 Studies on the nucleation and growth of metallic particles from supersaturated vapours. In *Shock Tube Research* (eds. J. L. Stollery, A. G. Gaydon and P. R. Owen), Proc. 8th Int. Shock Tube Symp. London: Chapman and Hall.

HONDA, M., TAKAYAMA, K., ONODERA, O. & KOHAMA, Y. 1975 Motion of reflected shock waves in shock tube. In *Modern Developments in Shock Tube Research* (ed. G. Kamimoto), Japan Shock Tube Res. Soc.

KERKER, M. 1969 *The Scattering of Light.* Academic Press.

LANDAU, L. D. & LIFSHITZ, E. M. 1959 *Fluid Mechanics*, p. 496. Pergamon.

LIESS, C. & DIDDEN, N. 1975 Experimentelle Untersuchungen von Ringwirbeln. In *Festschrift zum 50-jährigen Bestehen des Max-Planck-Instituts für Strömungsforschung* (eds. G. Grabitz and H. U. Vogel). Göttingen.

MAXWORTHY, T. 1977 Some experimental studies of vortex rings. *J. Fluid Mech.* **81**, 465–495.

MEIER, P. & SANDEMAN, R. J. 1975 Interferometric studies of shockwaves into argon up to 17 km/sec in the free piston double diaphragm shock tube. In *Modern Developments in Shock Tube Research* (ed. G. Kamimoto). Japan Shock Tube Res. Soc.

MIRELS, H. 1971 Boundary layer growth effects in shock tubes. In *Shock Tube Research* (ed. J. L. Stollery, A. G. Gaydon, P. R. Owen). London: Chapman and Hall.

OLSON, J. D. 1975 The refractive index and Lorenz–Lorentz function of fluid methane. *J. Chem. Phys.* **63**, 474–484.

OSHIMA, Y. & OSAKA, S. 1975 Interaction of two vortex rings moving side by side. *Nat. Sci. Rep. Ocharzonizu Univ.* **26**, 31–37.

SALTANOV, G. A., TSIKLAURI, G. V. & SHANIN, V. K. 1970 Shock waves in a flow of wet vapor with a high liquid phase content. *High Temperature* **8**, 533–539.

SPECKMANN, H.-D. 1978 Spontane Kondensation retrograder Gase durch Verdichtungsstöße. Diplomarbeit, Georg-August-Universität, Göttingen.

STURTEVANT, B. 1970 Lecture to the Division of Fluid Dynamics Meeting, American Physical Society. See also *Amer. Phys. Soc. Bull.* **15**, 1546.

THOMPSON, P. A. & BECKER, F. 1979 A one-parameter thermal-caloric corresponding-states model. *Chem. Eng. Science* **34**, 93–99.

THOMPSON, P. A. & SULLIVAN, D. A. 1975 On the possibility of complete condensation shock waves in retrograde fluids. *J. Fluid Mech.* **70**, 639–649.

WEGENER, P. P. 1969 Gas dynamics of expansion flows with condensation, and homogeneous nucleation of water vapor. In *Nonequilibrium Flows*, vol. I (ed. P. P. Wegener). New York: Marcel Dekker.

WEGENER, P. P. & WU, B. J. C. 1976 Homogeneous and binary nucleation: new experimental results and comparison with theory. *Faraday Disc. Chem. Soc.* no. 61, 77–82.

WHITE, D. R. 1961 Turbulent structure of gaseous detonation. *Phys. Fluids* **4**, 465–480.

WILSON, C. T. R. 1897*a* Condensation of water vapour in the presence of dust-free air and other gases. *Trans. Roy. Soc.* A **189**, 265–307.

WILSON, C. T. R. 1897*b* Kondensation des Wasserdampfes in Gegenwart von staubfreier Luft und anderen Gasen. *Beiblätter zu den Wiedemann Annalen der Physik und Chemie* **21**, 720–722.

YAMADA, T. 1973 An improved generalized equation of state. *A.I.Ch.E.J.* **19**, 286–291.

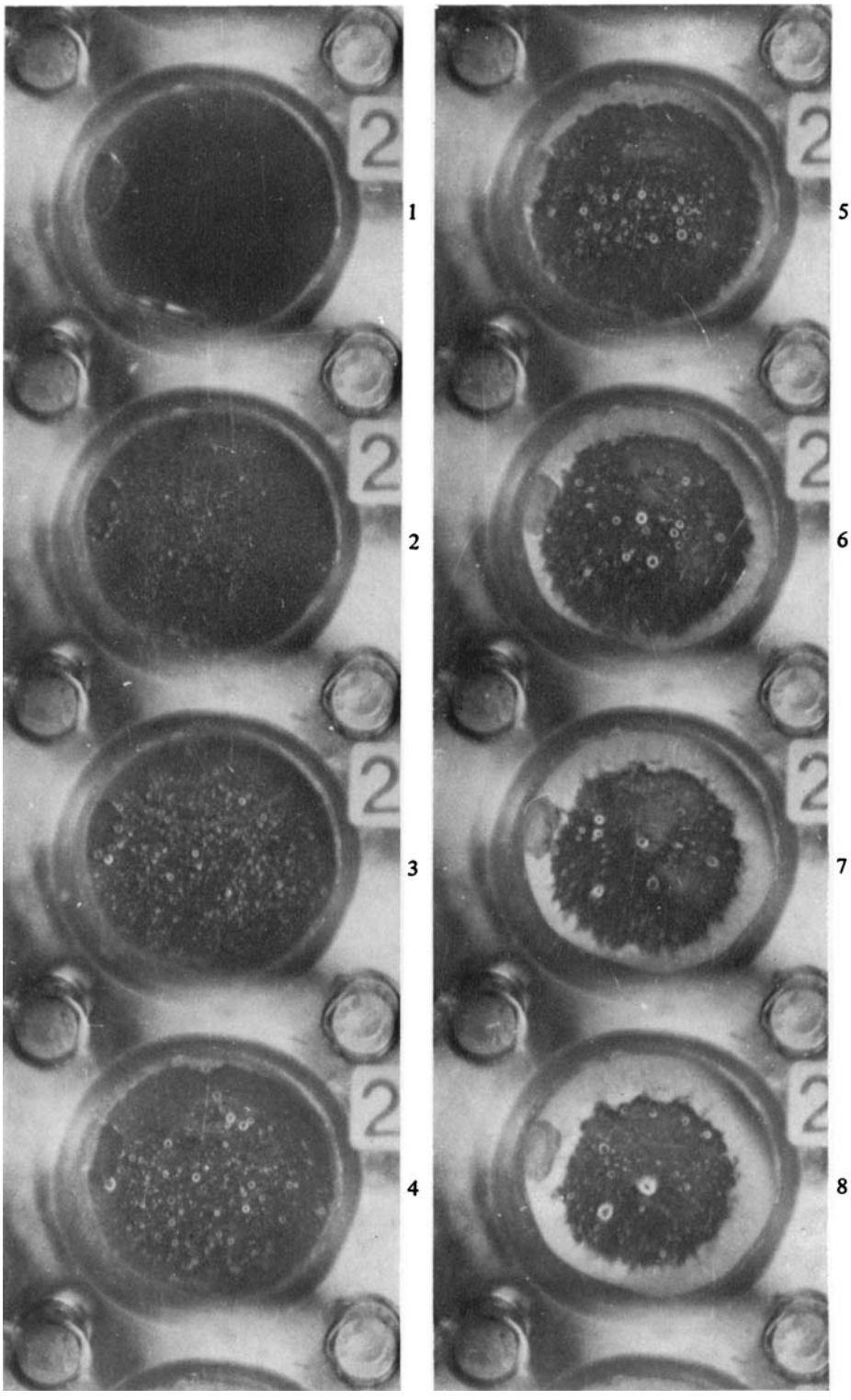

FIGURE 20(*a*). For legend see plate 2.

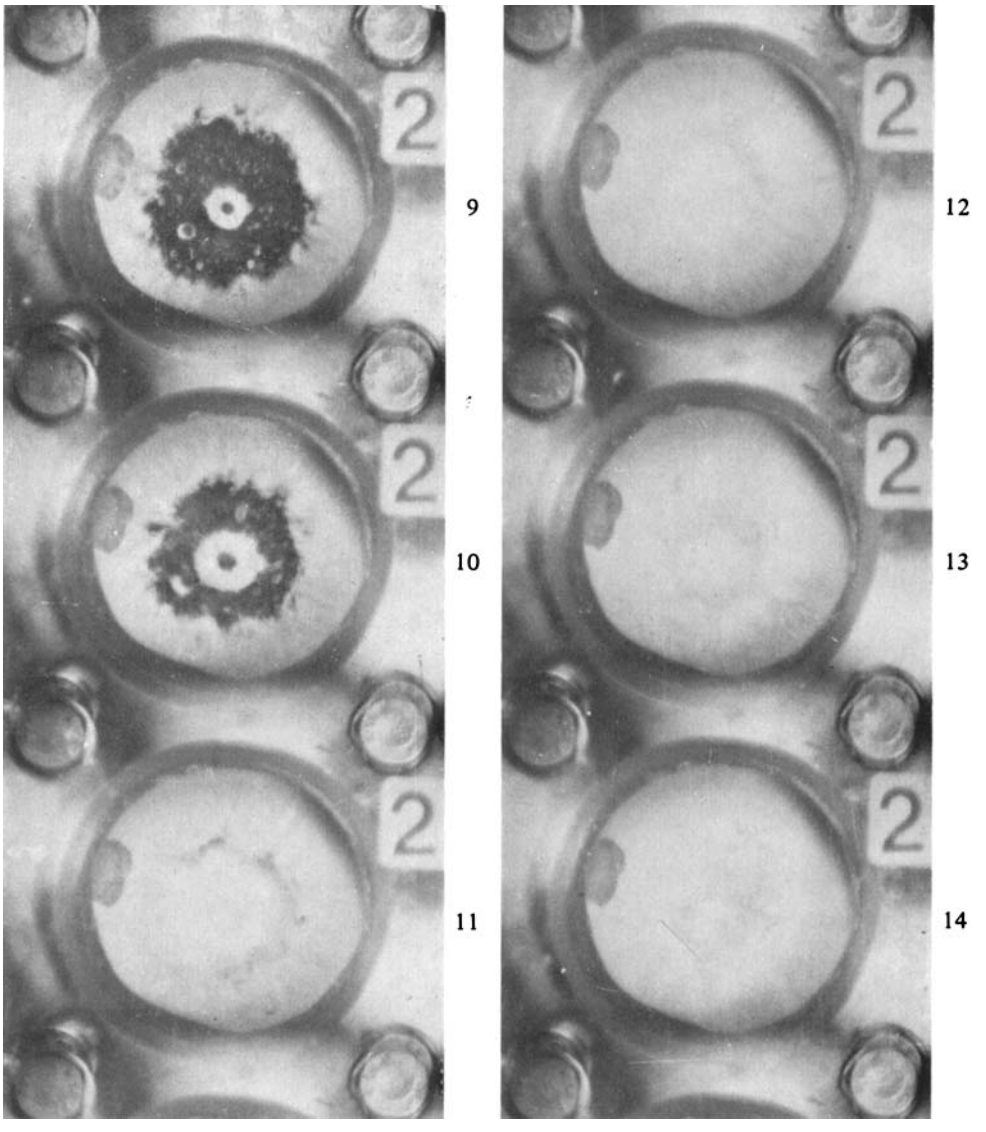

FIGURE 20. Consecutive frames 1–14 from high-speed motion pictures. Initial state in PP3: $T_0 = 130$ °C, $P_0 = 0{\cdot}67$ bar, $M_I = 2{\cdot}4$. Time interval between frames 0·137 ms. The irregular dark region on the left side is a crack in the glass window. Arrangement *B*. Window frame diameter 70 mm.

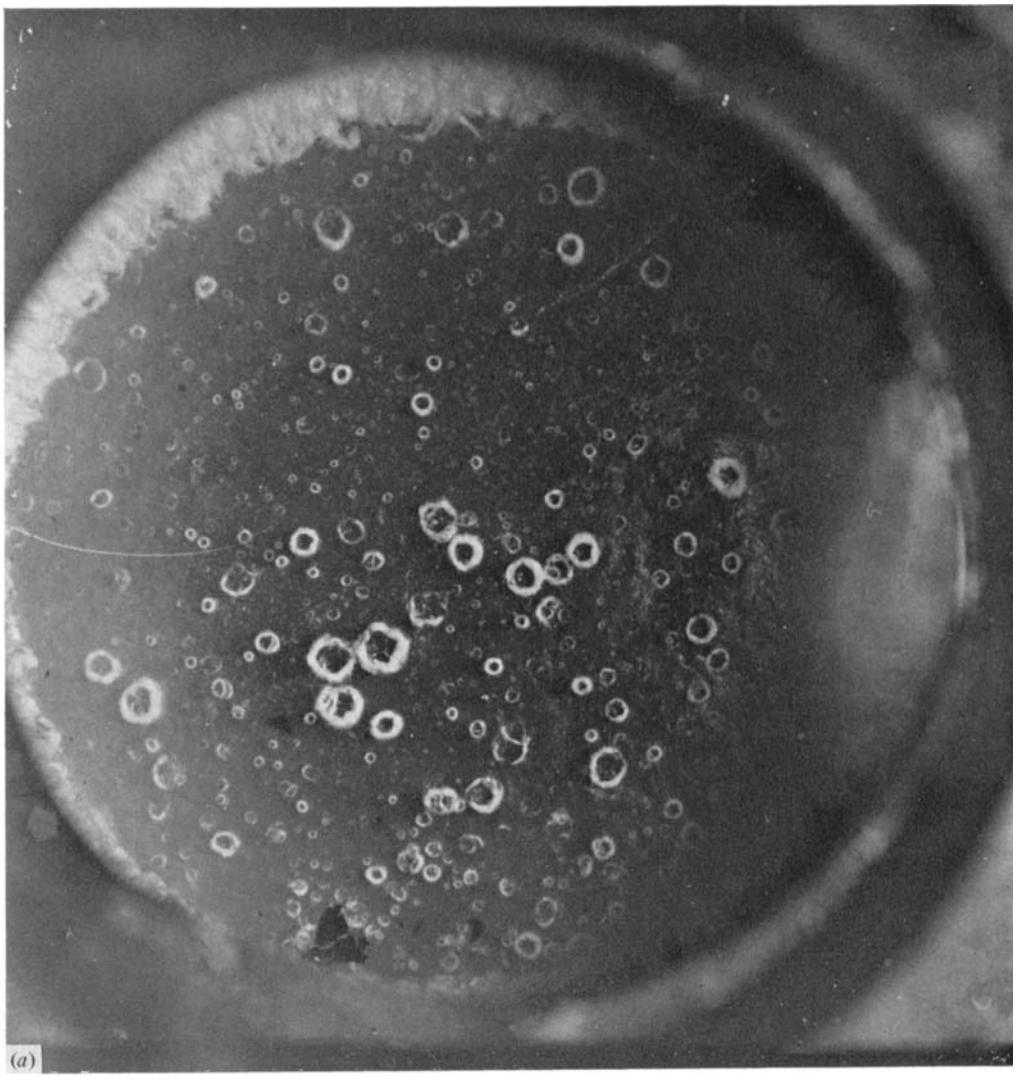

FIGURE 21. Ring objects behind the liquefaction shock under various conditions of illumination. PP3 with $T_0 = 130$ °C, $P_0 = 0{\cdot}67$ bar, $M_I = 2{\cdot}4$. (*a*) Lighting arrangement *B*, $t_R = 0{\cdot}54$ ms. Window frame diameter 70 mm. (*b*) Lighting arrangement *D*, $t_R = 0{\cdot}40$ ms. Window frame diameter 50 mm. (*c*) Arrangement *C*, $t_R = 0{\cdot}26$ ms. Reference line length 10 mm.

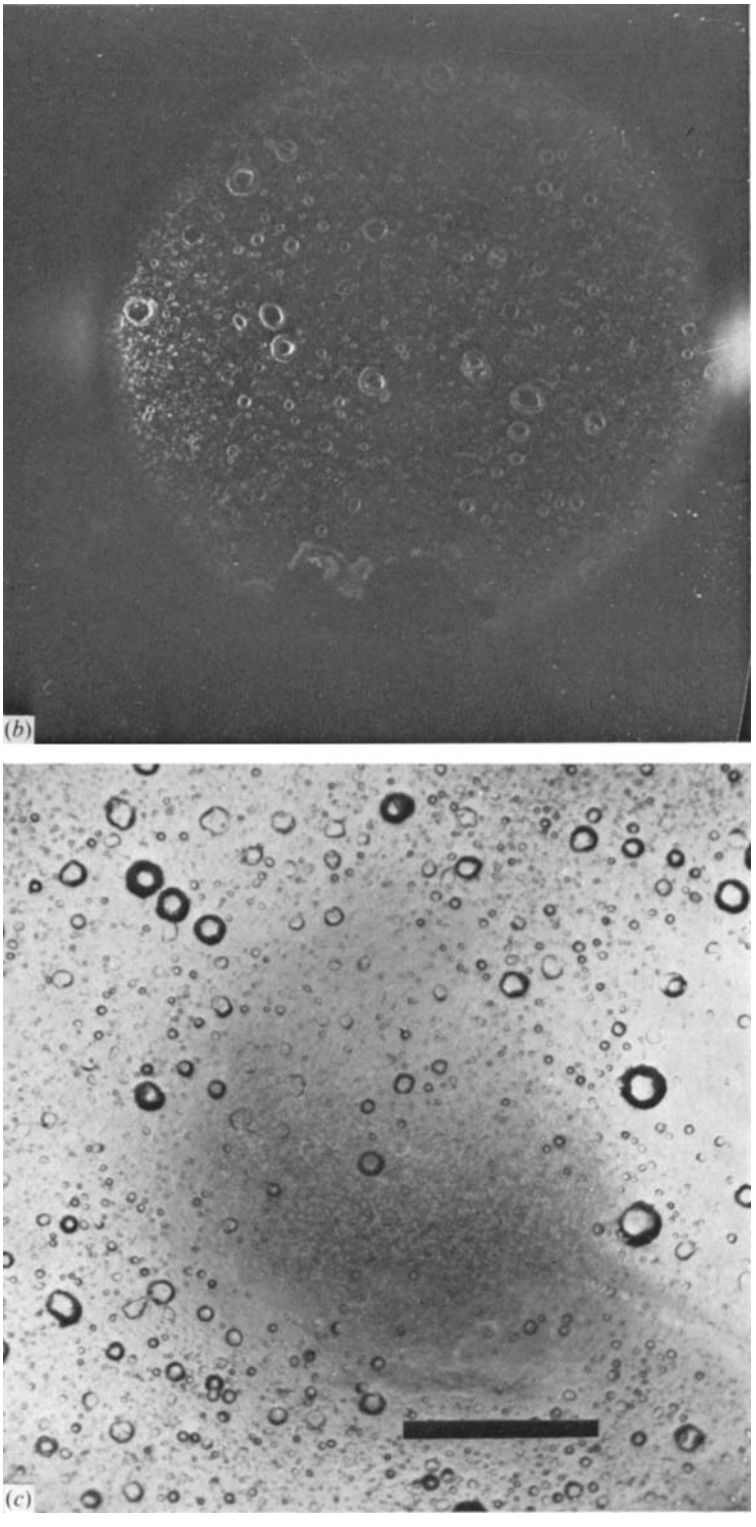

FIGURE 21 (*b*, *c*). For legend see plate 3.

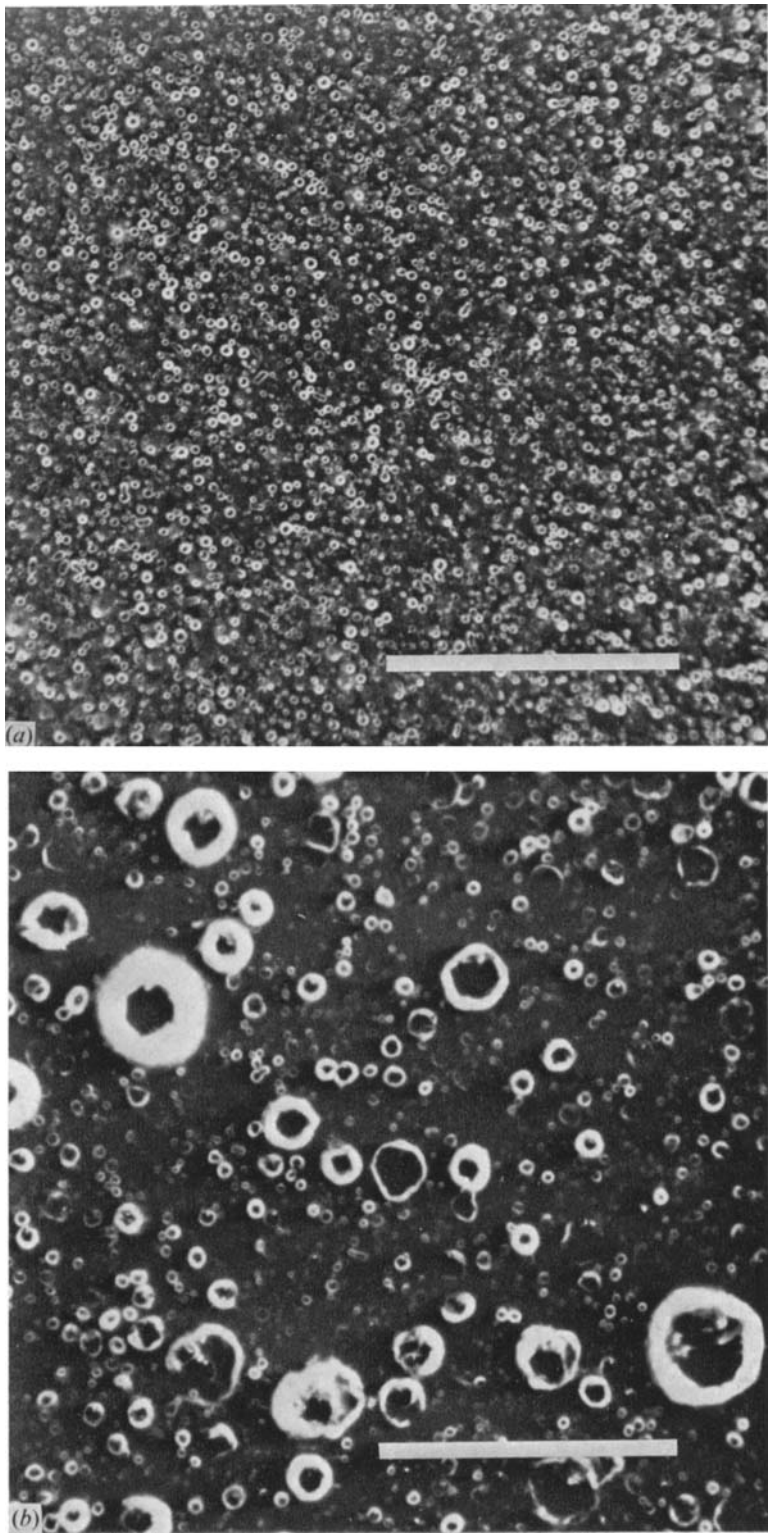

FIGURE 22. Ring objects at short and intermediate times after reflexion. PP3 with $T_0 = 130$ °C, $P_0 = 0{\cdot}67$ bar; $M_I = 2{\cdot}4$. Arrangement *B*. (*a*) $t_R = 0{\cdot}03$ ms, reference line length 5 mm. (*b*) $t_R = 0{\cdot}3$ ms, reference line length 10 mm.

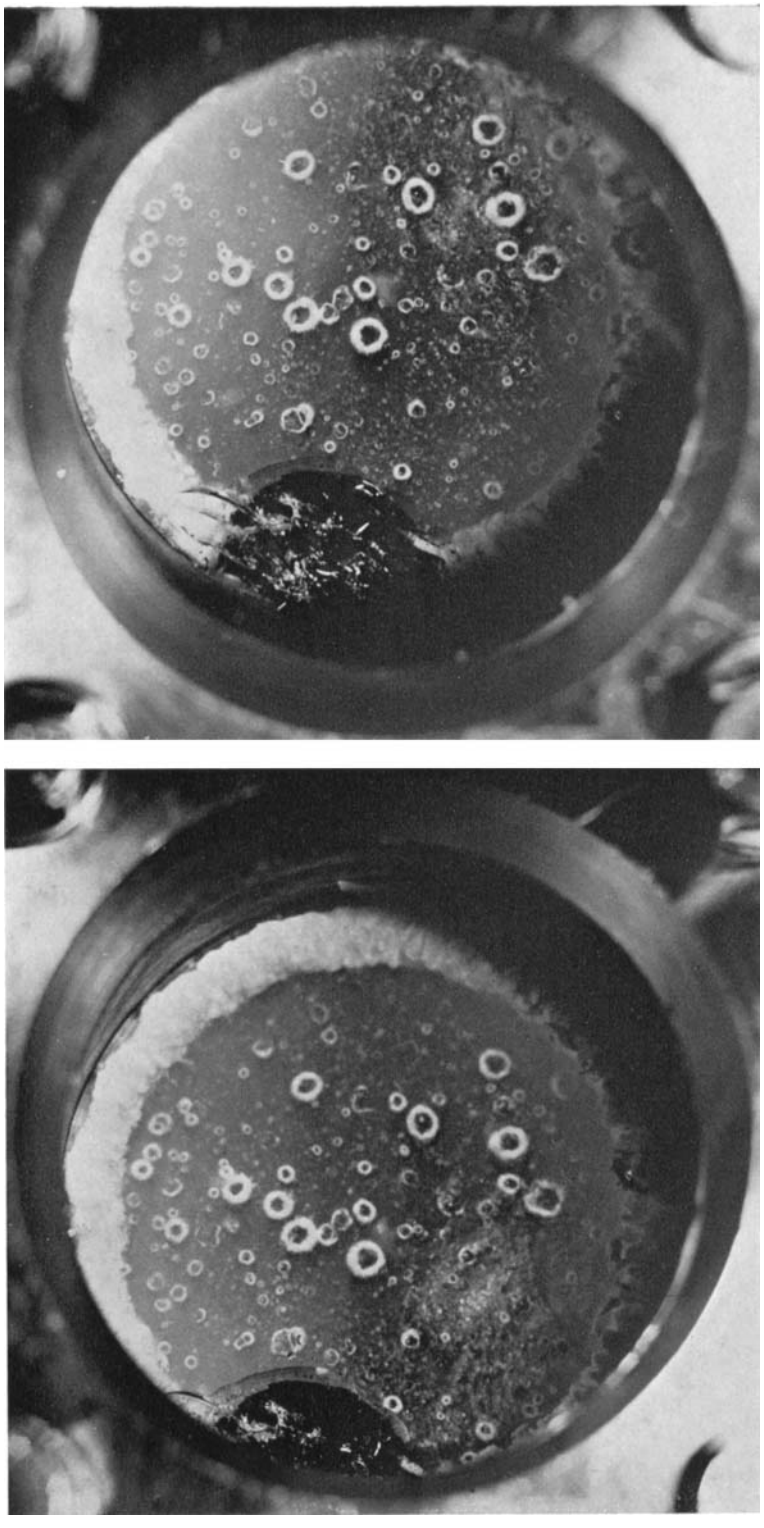

FIGURE 23. Stereoscopic photographs of the region behind the liquefaction shock. PP3 with $T_0 = 130$ °C, $P_0 = 0{\cdot}67$ bar; $M_I = 2{\cdot}4$, $t_R = 0{\cdot}60$ ms. Arrangement *E*. Frame diameter 70mm.

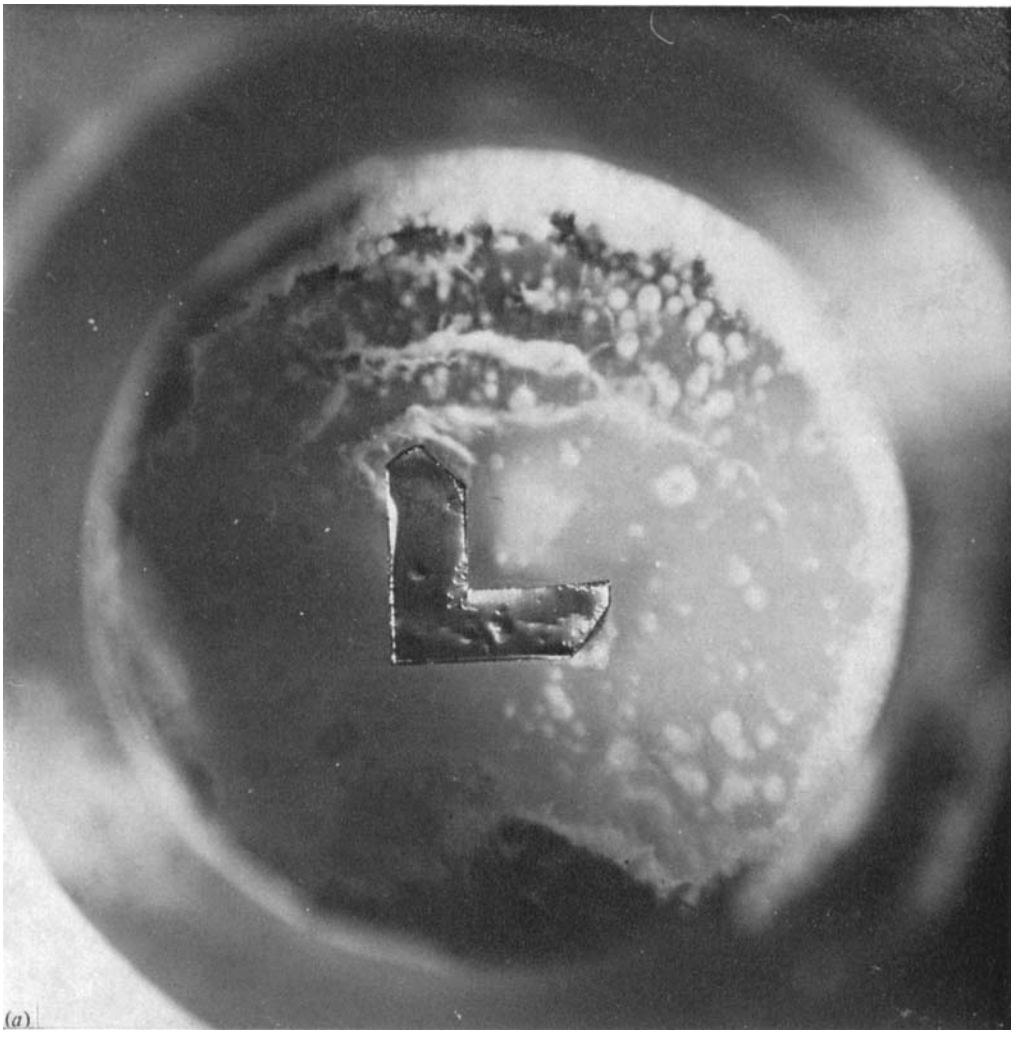

FIGURE 24. Liquefaction front with various conditions. (*a*) PP3, T_0 = 130 °C, P_0 = 0·99 bar, M_I = 2·05, equilibrium moisture y_1 = 15%. Lighting arrangement *B*, left-hand light only. Frame diameter 50 mm. (*b*) PP3, T_0 = 80 °C, P_0 = 0·24 bar, M_I = 2·70, y_1 = 16%. Lighting arrangement *B*. Frame diameter 70 mm. (*c*) FC-40, T_0 = 150 °C, P_0 = 0·33 bar, M_I = 2·50, y_1 = 27%. Arrangement *B*. Frame diameter 70 mm.

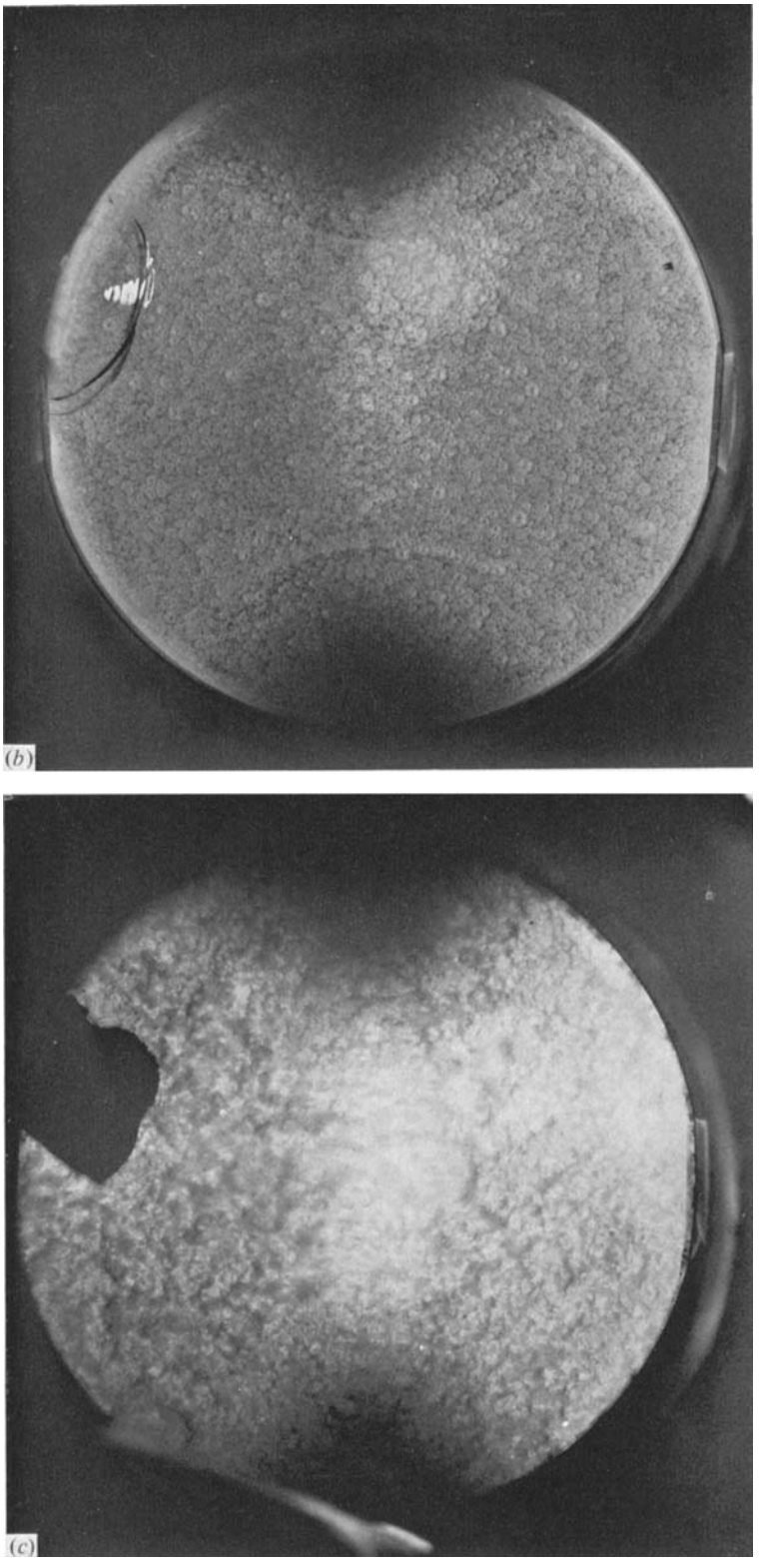

FIGURE 24(*b*, *c*). For legend see plate 7.

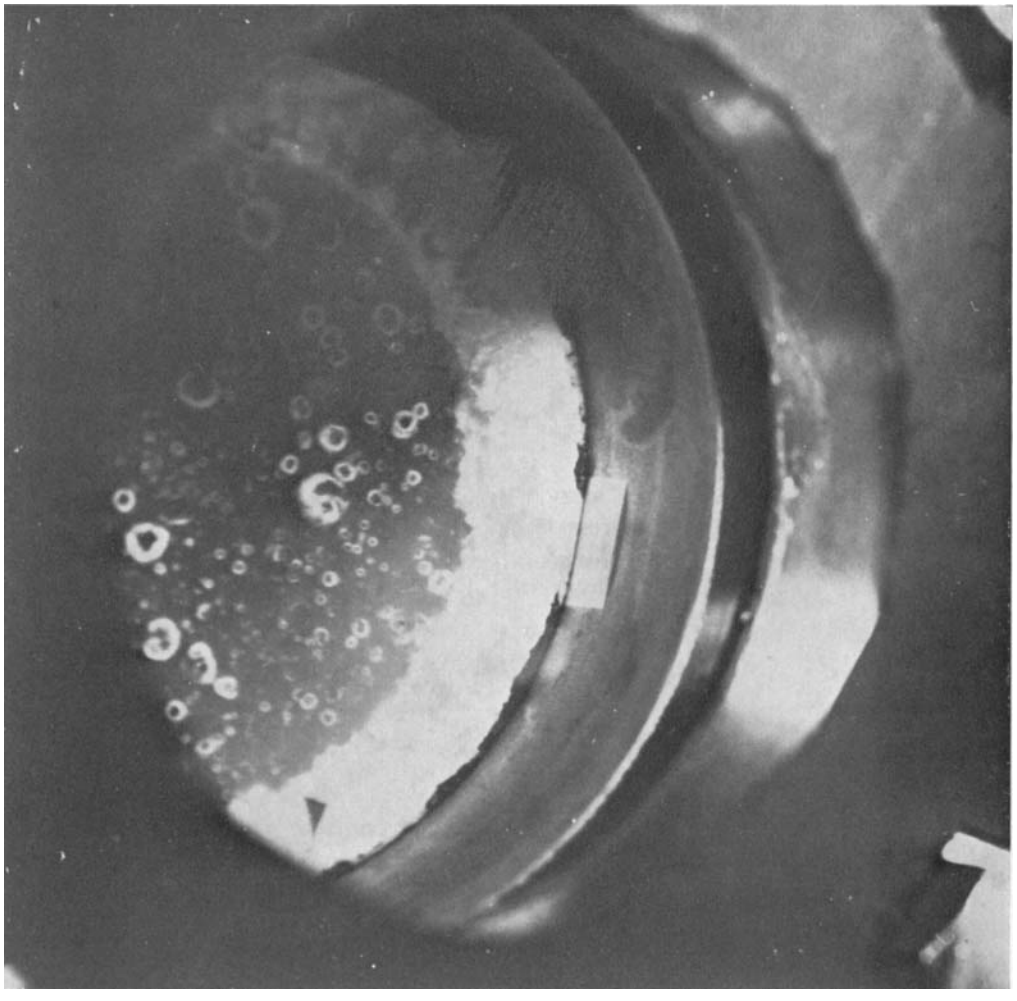

FIGURE 26. Oblique view of the corner vortex structure. PP3, $T_0 = 130$ °C, $P_0 = 0{\cdot}67$ bar, $M_I = 2{\cdot}4$, $t_R = 0{\cdot}73$ ms. Arrangement F.